



Quantification of trans-Atlantic dust transport from seven-year (2007–2013) record of CALIPSO lidar measurements



Hongbin Yu^{a,b,*}, Mian Chin^b, Huisheng Bian^{b,c}, Tianle Yuan^{b,c}, Joseph M. Prospero^d, Ali H. Omar^e, Lorraine A. Remer^c, David M. Winker^e, Yuekui Yang^{b,f}, Yan Zhang^{b,f}, Zhibo Zhang^g

^a Earth System Science Interdisciplinary Center, University of Maryland, College Park, MD, USA

^b Earth Sciences Division, NASA Goddard Space Flight Center, Greenbelt, MD, USA

^c Joint Center for Earth Science and Technology, University of Maryland at Baltimore County, Baltimore, MD, USA

^d Cooperative Institute for Marine and Atmospheric Studies, Rosenstiel School of Marine and Atmospheric Science, University of Miami, Miami, FL, USA

^e NASA Langley Research Center, Hampton, VA, USA

^f Universities Space Research Association, Columbia, MD, USA

^g Department of Physics, University of Maryland at Baltimore County, Baltimore, MD, USA

ARTICLE INFO

Article history:

Received 3 September 2014

Received in revised form 10 December 2014

Accepted 14 December 2014

Available online 8 January 2015

Keywords:

Aerosol

Dust

Transport

CALIPSO

Satellite

ABSTRACT

The trans-Atlantic dust transport has important implications for human and ecosystem health, the terrestrial and oceanic biogeochemical cycle, weather systems, and climate. This study provides an observation-based multiyear estimate of trans-Atlantic dust transport using a 7-year (2007–2013) record of the Cloud-Aerosol Lidar with Orthogonal Polarization (CALIOP) measurements of the three dimensional distribution of aerosol backscatter, extinction and depolarization ratio in both cloud-free and above-cloud conditions. We estimate that on a basis of the 7-year average and integration over 10°S–30°N, 182 Tg a⁻¹ dust leaves the coast of North Africa at 15°W, of which 132 Tg a⁻¹ and 43 Tg a⁻¹ reaches 35°W and 75°W, respectively. These flux estimates have an overall known uncertainty of ±(45–70)%. Because of lack of reliable observations, uncertainties associated with the diurnal variation of dust and the missing below-cloud dust cannot be quantified. Significant seasonal variations are observed in both the magnitude of total dust mass flux and its meridional and vertical distributions. The interannual variability of annual dust mass flux is highly anti-correlated with the prior-year Sahel Precipitation Index. Using only cloud-free aerosol observations to calculate dust mass flux could introduce a high bias when compared with all-sky conditions that include both cloud-free and above-cloud aerosol observations. The bias is about 20% at 35°W and 75°W in boreal winter and spring based on the 7-year average, as long as dust within and below low-level clouds is negligible.

© 2014 Elsevier Inc. All rights reserved.

1. Introduction

The trans-Atlantic transport of dust has gained tremendous attention over past several decades, because of various far-reaching impacts of dust (and associated microorganisms) on human and ecosystem health (Griffin, 2007; Prospero, 1999; Prospero, Blades, Mathison, & Naidu, 2005; Prospero, Collard, Molinié, & Jeannot, 2014), terrestrial and oceanic biogeochemical cycle (Jickells et al., 2005; Mahowald et al., 2008; Prospero et al., 1996; Swap, Garstang, Greco, Talbot, & Källberg, 1992; Swap, Ulanski, Cobbett, & Garstang, 1996), weather systems (Dunion & Velden, 2004), and climate (Evan, Vimont, Heidinger, Kossin, & Bennartz, 2009; Wilcox, Lau, & Kim, 2010). The dust cycle has become an emerging core theme of Earth system science (Shao et al., 2011). Model simulation is an essential tool to quantify the

transport of dust but is currently highly uncertain (e.g., Huneus et al., 2011; Kim et al., 2014; Prospero, Landing, & Schulz, 2010). There is a pressing need to evaluate and constrain model simulations with reliable observations and assess a variety of environmental influences of dust with a higher level of confidence.

Satellite observations, alone or in combination with surface and aircraft observations, are ideal for studying the trans-continental transport of aerosols, owing to their inherent advantages of routine sampling and large spatial and temporal coverage. In particular, significant progress in satellite remote sensing of aerosol properties in the last two decades offers the opportunity to increase quantitative characterization and estimates of aerosol transport in addition to qualitative tracking of aerosol plumes (Yu, Remer, Kahn, Chin, & Zhang, 2013). Voluminous studies have used satellite observations to characterize specific dust transport events and episodes, or provide insight into seasonal and inter-annual variation of dust transport (e.g., Adams, Prospero, & Zhang, 2012; Ben-Ami, Koren, & Altaratz, 2009; Ben-Ami, Koren, Altaratz, & Lehahn, 2012; Ben-Ami et al., 2010; Chiappello, Moulin, & Prospero, 2005;

* Corresponding author at: NASA GSFC Code 613, Greenbelt, MD 20771, USA. Tel.: +1 301 614 6209.

E-mail address: Hongbin.Yu@nasa.gov (H. Yu).

Doherty, Riemer, & Hameed, 2012; Generoso, Bey, Labonne, & Bréon, 2008; Guo et al., 2013; Huang, Zhang, & Prospero, 2010; Kalashnikova & Kahn, 2008; Kim et al., 2014; Liu et al., 2008; Moulin, Lambert, Dulac, & Dayan, 1997; Peyridieu et al., 2010; Ridley, Heald, & Ford, 2012; Riemer, Doherty, & Hameed, 2006; Su & Toon, 2011; Swap et al., 1996; Yu et al., 2010, 2013). These studies have progressed from qualitatively following an aerosol plume across the ocean basin, to quantitatively characterizing the evolution of particle properties and height. Furthermore a few studies in recent years have taken advantage of the advances in aerosol remote sensing to translate measurements of aerosol optical depth (AOD) to aerosol mass, with the help of observed particle properties (e.g., size and shape) and assumed plume heights, and then estimate the mass flux of the particles that depart from one continent and arrive at another (Kaufman et al., 2005; Koren et al., 2006; Rudich, Kaufman, Dayan, Yu, & Kleidman, 2008; Yu, Remer, et al., 2012; Yu et al., 2008). These studies have offered important insights into aerosol intercontinental transport and its impacts on air quality, climate change, and biogeochemical cycles.

The satellite-based dust flux estimate is subjected to large uncertainties because of uncertainties associated with derived dust optical depth (DOD) itself (Yu et al., 2009, 2013), dust mass extinction efficiency (MEE) that converts DOD to dust mass loading (Kaufman et al., 2005), and assumptions about the dust transport height (Schepanski, Tegen, & Macke, 2009). In particular, in the original MODIS-based estimate of trans-Atlantic dust transport (Kaufman et al., 2005), no adequate data were available at that time to characterize the dust transport heights. Instead the authors had to rely on a correlative analysis between MODIS AOD and wind speed at different layers over the eastern tropical Atlantic to infer the transport heights (Kaufman et al., 2005). They found that AOD has the highest correlation with wind speed at 700 hPa in summer and at 850 hPa in winter, which was used as an approximation for the dust transport height. While a reasonable seasonality of the transport height was accounted for, spatial variation of dust layer height during the cross-ocean transport was not considered. Because of the simplified characterization of aerosol vertical distribution, the MODIS-based estimate did not provide the profile of dust mass flux. Similar to other satellite-based estimates of aerosol mass fluxes, it was also assumed that MODIS observed aerosols in cloud-free conditions represent cloudy conditions well, which has not been assessed or justified by observations (Yu et al., 2008).

This study aims to assess these assumptions and provide an independent estimate of vertically resolved trans-Atlantic dust transport with a multi-year dataset of the three-dimensional distribution of dust aerosol from the Cloud-Aerosol Lidar with Orthogonal Polarization (CALIOP) onboard the Cloud-Aerosol Lidar and Infrared Pathfinder Satellite Observations (CALIPSO). CALIOP has been providing measurements of aerosol backscatter, extinction and depolarization profiles over a global scale since June 2006 (Winker et al., 2009). The depolarization measurements allow for a separation of mineral dust from other types of aerosol, because mineral dust is largely coarse in size and non-spherical and has much larger depolarization ratio than largely spherical particles (e.g., marine, pollution, and smoke aerosols). CALIOP is also capable of detecting aerosol layers above low-level clouds (Winker et al., 2013; Yu & Zhang, 2013; Yu, Zhang, et al., 2012). This new observing capability of above-cloud aerosol (ACA) profiles provides a first-ever opportunity of examining the representativeness of clear-sky aerosol (CSA) observations for cloudy-sky conditions and its effect on the flux estimate (Yu et al., 2013), at least to some extent, because CALIOP still cannot detect aerosol layers below optically thick low-level clouds. The remainder of the paper is organized as follows. Section 2 describes the approach of estimating dust mass fluxes from CALIOP measurements. Section 3 presents the CALIOP-based dust flux estimates and comparisons with the MODIS-based estimates. Various sources of uncertainty associated with the dust flux estimate are discussed in Section 4. Concluding remarks are given in Section 5.

2. Description of approach

This study uses CALIPSO version 3, level 2 lidar data of aerosol profiles and cloud layers at a nominal resolution of 5 km along the track and covering a 7-year period from December 01, 2006 to November 30, 2013. The aerosol profile has a vertical resolution of 60 m up to 20.2 km and changes to 180 m from 20.2 to 30.1 km. The cloud layer product is used to determine if the column is cloud free or not and at what altitude the clouds reside. Several quality control procedures are applied to remove low quality data in our analysis. Only nighttime data are used because the interference of sunlight during the day degrades the quality of daytime data. Following Yu et al. (2010) and Winker et al. (2013), CALIOP data are screened with quality flags embedded in the level 2 aerosol product. A cloud-aerosol discrimination (CAD) score is used to indicate the confidence in the classification of a layer feature as either aerosol or cloud. In this study, we selected layers with CAD scores between -20 and -100 to avoid low-confidence aerosol-cloud discrimination (Yu et al., 2010). The extinction quality control flag (Ext_QC) flag is provided to indicate problematic retrievals. In this study only layers with Ext_QC values of 0, 1, 18, and 16 are selected (Winker et al., 2013).

To assess the cross-ocean transport of dust, we focus on zonal transport at three longitudinal cross sections across the tropical/sub-tropical Atlantic Ocean, as illustrated in Fig. 1: 10° – 20° W, 30° – 40° W, and 70° – 80° W (for brevity, they are referred to as 15° W, 35° W, and 75° W cross section, respectively), the same as that used in Kaufman et al. (2005). The three cross sections are selected to respectively capture the dust outflow adjacent to North Africa, the dust inflow to South America, and the dust inflow into the Caribbean Sea. CALIOP aerosol data during a season (i.e., December–January–February or DJF, March–April–May or MAM, June–July–August or JJA, September–October–November or SON) are aggregated into 10° (longitude) \times 10° (latitude) boxes along the three longitudinal cross sections. Note that DJF represents the December from the previous year, and January and February from the current year. Aerosol profiles are first categorized into two groups, namely CSA and ACA, as illustrated in Fig. 2. Similar to that in Yu et al. (2010), CSA includes columns that are completely cloud-free or with the presence of optically thin (optical depth < 0.2) and high-level (cloud base > 7 km) clouds. We found that the seasonal-average aerosol extinction profile in the presence of the optically thin and high-level clouds does not differ significantly from that in completely cloud-free conditions. The inclusion of columns with optically thin and high-level clouds increases the sampling. ACA includes columns with single-layer, low-level clouds with a top lower than 4 km. Fig. 3 shows the fraction of occurrence of ACA (f_{ACA}) detected by CALIOP in the nighttime data base, indicating significant seasonal, interannual, and geographical variations.

For each aerosol backscatter coefficient (at 532 nm, $\text{km}^{-1} \text{sr}^{-1}$) profile, we derive the ratio of dust to total backscatter (f_d) at each altitude by using the CALIOP observed particulate depolarization ratio (δ) and a priori knowledge of depolarization ratios of dust (δ_d) and non-dust (δ_{nd}) aerosols as follows (Hayasaka et al., 2007):

$$f_d = \frac{(\delta - \delta_{nd})(1 + \delta_d)}{(1 + \delta)(\delta_d - \delta_{nd})}. \quad (1)$$

The value of f_d is set at 1 if $f_d > 1$ and at 0 if $f_d < 0$. The dust backscatter coefficient ($\text{m}^{-1} \text{sr}^{-1}$) profiles are thus derived from the profiles of total backscatter and calculated f_d . By assuming a dust extinction-to-backscatter ratio (lidar ratio) of 40 sr at 532 nm, based on observations in the region (Omar et al., 2010), we obtain dust extinction coefficient (m^{-1}) profiles. Here we do not derive dust extinction from the total extinction, because converting backscatter f_d to that for extinction requires an assumption of lidar ratios for both dust and non-dust aerosols. In the tropical Atlantic Ocean, the non-dust aerosol is a mixture of marine aerosol and biomass burning smoke, two types of particles with

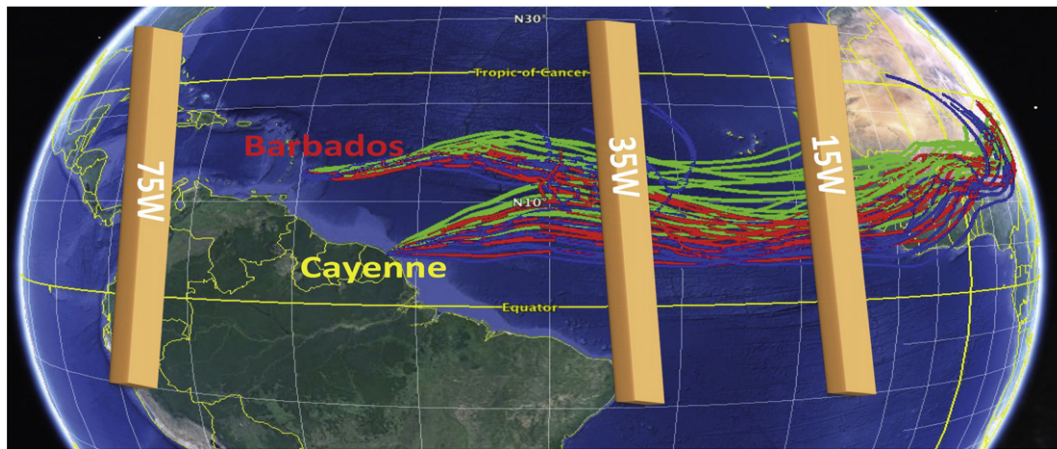


Fig. 1. Illustration of three cross sections centered at 15°W, 35°W, and 75°W that are used to calculate dust mass flux in zonal direction. The background map shows HYSPLIT (Draxler & Rolph, 2014) 27-member ensemble 10-day back trajectories originating from Barbados (13.17°N, 59.43°W) and Cayenne (04.95°N, 52.31°W) at 0600 UTC April 2, 2010. On April 2, 2010, Barbados recorded dust surface concentration of $155 \mu\text{g m}^{-3}$, while Cayenne recorded PM_{10} concentration of $179 \mu\text{g m}^{-3}$ (Prospero et al., 2014). Such extremely high concentrations of particles in both locations were traced back to similar source regions in North Africa.

distinctly different lidar ratios (Omar et al., 2009) resulting in varying fractional contributions that depend on season and location (Ben-Ami et al., 2012; Yu et al., 2009). Because of these complexities, assuming a single non-dust lidar ratio could introduce additional uncertainty and is thus avoided in this study.

Thus in this study we avoid assumptions of non-dust lidar ratio, but rely on assumptions of lidar ratio for dust, and values for depolarization ratio of dust and non-dust (δ_d and δ_{nd}). We use a priori available observations of depolarization ratio of known dust and known non-dust to set the thresholds of δ_d and δ_{nd} . Although marine aerosol and urban haze are highly hygroscopic and generally have very low depolarization ratio, some types of non-dust aerosols may have non-negligible depolarization ratio. For example, biomass-burning smoke (Burton et al., 2012; Fiebig et al., 2002), sea-salt crystals and ammonium sulfate crystals (Sakai, Nagai, Zaizen, & Mano, 2010) can have a depolarization ratio of about 0.07. Given these observations, we use 0.02 and 0.07 as lower and upper bounds for δ_{nd} in this study. Mineral dust has a much higher

depolarization ratio than non-dust aerosols. Observations off the coast of North Africa show that Saharan dust has a depolarization ratio of about 0.3 (Ansmann, Seifert, Tesche, & Wandinger, 2012; Esselborn et al., 2009; Freudenthaler et al., 2009). A laboratory study (Sakai et al., 2010) shows that the depolarization ratio of dust can decrease significantly with decreasing particle size, suggesting that the dust in the western tropical Atlantic, where particle size is smaller after transport, may have a smaller value of depolarization ratio than that in the eastern tropical Atlantic closer to sources. On the other hand, spherical particles have larger sedimentation velocity than do non-spherical particles (Cheng, Yeh, & Allen, 1988), resulting in an increase of depolarization ratio during the westward transport of Saharan dust (Reid et al., 2003; Yang, Marshak, Kostinski, & Várnai, 2013). To encompass these variations, in this study we assume 0.3 and 0.2 to represent the upper and lower bounds of δ_d , respectively. Fig. 4 shows seasonal average DODs over $21 10^\circ \times 10^\circ$ segments for 2007, which are derived with four sets of (δ_d , δ_{nd}) combining their upper and low bounds. Clearly using the criteria of $\delta_d = 0.30$ and $\delta_{nd} = 0.07$ yields the lowest dust fraction and DOD, while using $\delta_d = 0.20$ and $\delta_{nd} = 0.02$ the highest dust fraction and DOD. For convenience, we label these scenarios as “lower-bound dust fraction” (LDF) and “upper-bound dust fraction” (UDF), respectively. For the two other scenarios using the criteria of $\delta_d = 0.30$ and $\delta_{nd} = 0.02$ or $\delta_d = 0.20$ and $\delta_{nd} = 0.07$, the dust fraction and DOD fall in between the LDF and UDF values and hence will not be discussed further.

After achieving dust fraction, extinction and DOD, we then derive profiles of dust mass concentration (m , unit: g m^{-3}) from the dust extinction profiles by using the dust MEE of $0.37 \text{ m}^2 \text{ g}^{-1}$ at 532 nm, the same as that used in Kaufman et al. (2005). Here dust is assumed to be hydrophobic and does not change its size distribution during the course of transport from the coast near North Africa to the Caribbean Sea. While these assumptions for MEE facilitate a comparison of CALIOP dust mass fluxes with the MODIS estimates, we will discuss sensitivity of the dust mass flux to MEE in Section 4. The dust mass flux rate (g s^{-1}) in the zonal (east–west) direction is calculated separately for CSA (FR_{CSA}) and ACA (FR_{ACA}) as follows:

$$\text{FR}_{\text{CSA}} = - \int_0^{10\text{km}} m(z) U_{\text{CLR}}(z) L dz \quad (2)$$

$$\text{FR}_{\text{ACA}} = - \int_{Z_t}^{10\text{km}} m(z) U_{\text{CLD}}(z) L dz \quad (3)$$

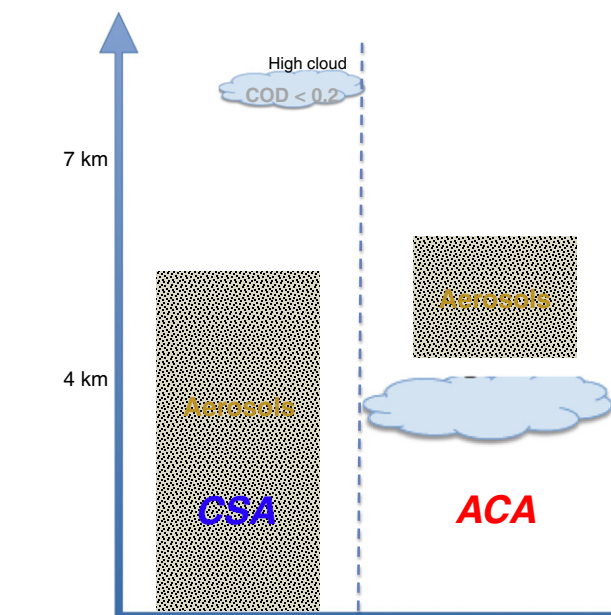


Fig. 2. Illustration of categorizing CALIOP observations of aerosol profiles into clear-sky aerosol (CSA) and above-cloud aerosol (ACA).

where $m(z)$ is the mass concentration at altitude z , Z_t is seasonally averaged low-level cloud-top, L is the length (m) of a 10° latitude segment

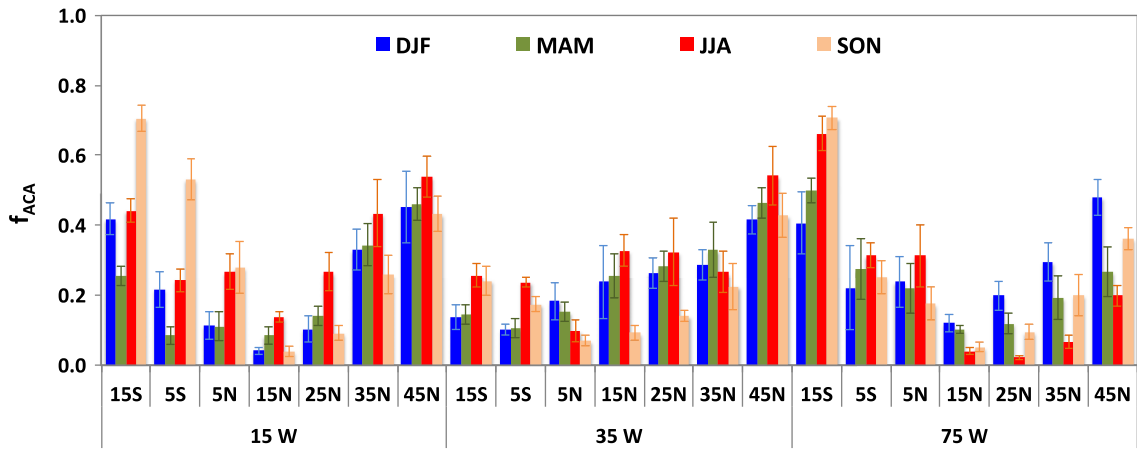


Fig. 3. CALIOP detected ACA occurrence fraction (f_{ACA}) in different seasons (distinguished by color) and regions. The wide bar represents the 7-year average, with error bar indicating the standard deviation over the 7-year period.

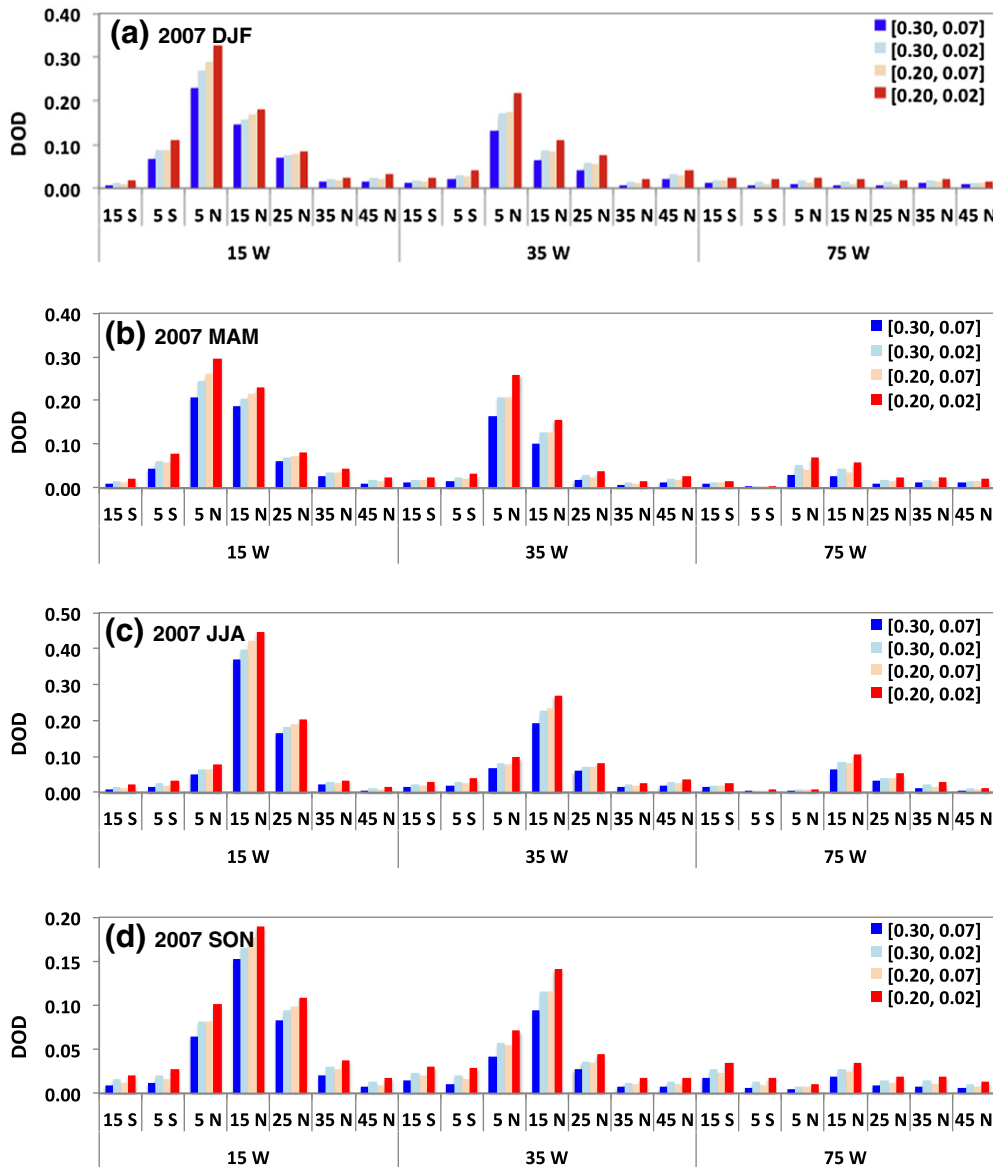


Fig. 4. Seasonal average DOD for CSA in individual $10^\circ \times 10^\circ$ segments (with central latitude and longitude labeled) in (a) DJF, (b) MAM, (c) JJA, and (d) SON of 2007. DOD is derived with 4 sets of $[\delta_a, \delta_{nd}]$ thresholds (see legend). The blue and red corresponds to the LDF and UDF scenarios, respectively, as discussed in the text.

along a longitude line, and U_{CLR} and U_{CLD} are the zonal wind speed ($m\ s^{-1}$) in “clear” and “cloudy” conditions respectively, which are taken from MERRA assimilated meteorological fields (Rienecker et al., 2011) by broadly categorizing “clear” and “cloudy” using a cloud fraction threshold of 0.3. The negative sign is applied in Eqs. (2) and (3) so that the westward transport has a positive flux and the eastward transport has a negative flux, opposite to the general definition of the wind directions. The dust mass flux rate in the all-sky condition (FR_{ALL}) is computed as an average of FR_{CSA} and FR_{ACA} weighted by the fraction of CSA (f_{CSA}) and ACA ($f_{ACA} = 1 - f_{CSA}$), respectively:

$$FR_{ALL} = FR_{CSA} f_{CSA} + FR_{ACA} (1 - f_{CSA}). \quad (4)$$

Seasonal dust mass fluxes (F_{CSA} , F_{ACA} , and F_{ALL} , unit: g) are then calculated by multiplying corresponding seasonal average flux rate with the duration of time (s). Here it is assumed that aerosols below the clouds, which cannot be detected by CALIOP, make negligible contribution to the flux.

3. Results

3.1. CALIOP AOD and dust fraction

Based on the methods and assumptions described in Section 2, we calculate the seasonal mean vertical profiles of total and dust extinction

coefficient (km^{-1}) averaged over 10° – $20^{\circ}N$ at the cross section of $15^{\circ}W$, $35^{\circ}W$, and $75^{\circ}W$ in MAM 2012 (see Fig. 5). Similar profiles in JJA 2012 are shown in Fig. 6. In these figures, both CSA (blue) and ACA (red) profiles are shown and dust is separated from non-dust aerosol in the LDF (dotted line) and UDF (solid line) scenarios. In both seasons, total extinction profiles (top panels) for CSA show a spike at an altitude of 200–300 m, presumably an indicator of contribution by marine aerosols. These spikes are substantially reduced in the dust extinction profiles (bottom panels). In general, dust plumes are higher in JJA than MAM, which is generally consistent with seasonal variations from previous studies (e.g., Ben-Ami et al., 2012; Chiapello et al., 1997; Huang et al., 2010; Kalu, 1979; Yu et al., 2010). It also shows that while the dust plumes remain at a relatively constant height or subside slightly east of $35^{\circ}W$, they descend significantly west of $35^{\circ}W$, which underlines the importance of accounting for the descending plumes when calculating the dust transport fluxes. In both seasons, the top of the dust plume for ACA is higher than that for CSA, in particular at $15^{\circ}W$ and $35^{\circ}W$. When integrating dust extinction in the vertical, DOD for ACA is much smaller than that for CSA at $35^{\circ}W$ and $75^{\circ}W$. At $15^{\circ}W$, DOD for ACA is higher than or close to that for CSA in MAM and JJA, respectively, although CALIOP does not detect aerosols within and below clouds. Comparisons between UDF (solid line) and LDF (dotted line) dust extinction profiles show that dust and non-dust separation at $35^{\circ}W$ and $75^{\circ}W$ is more sensitive to the depolarization criteria in the atmospheric boundary layer than in the free troposphere.

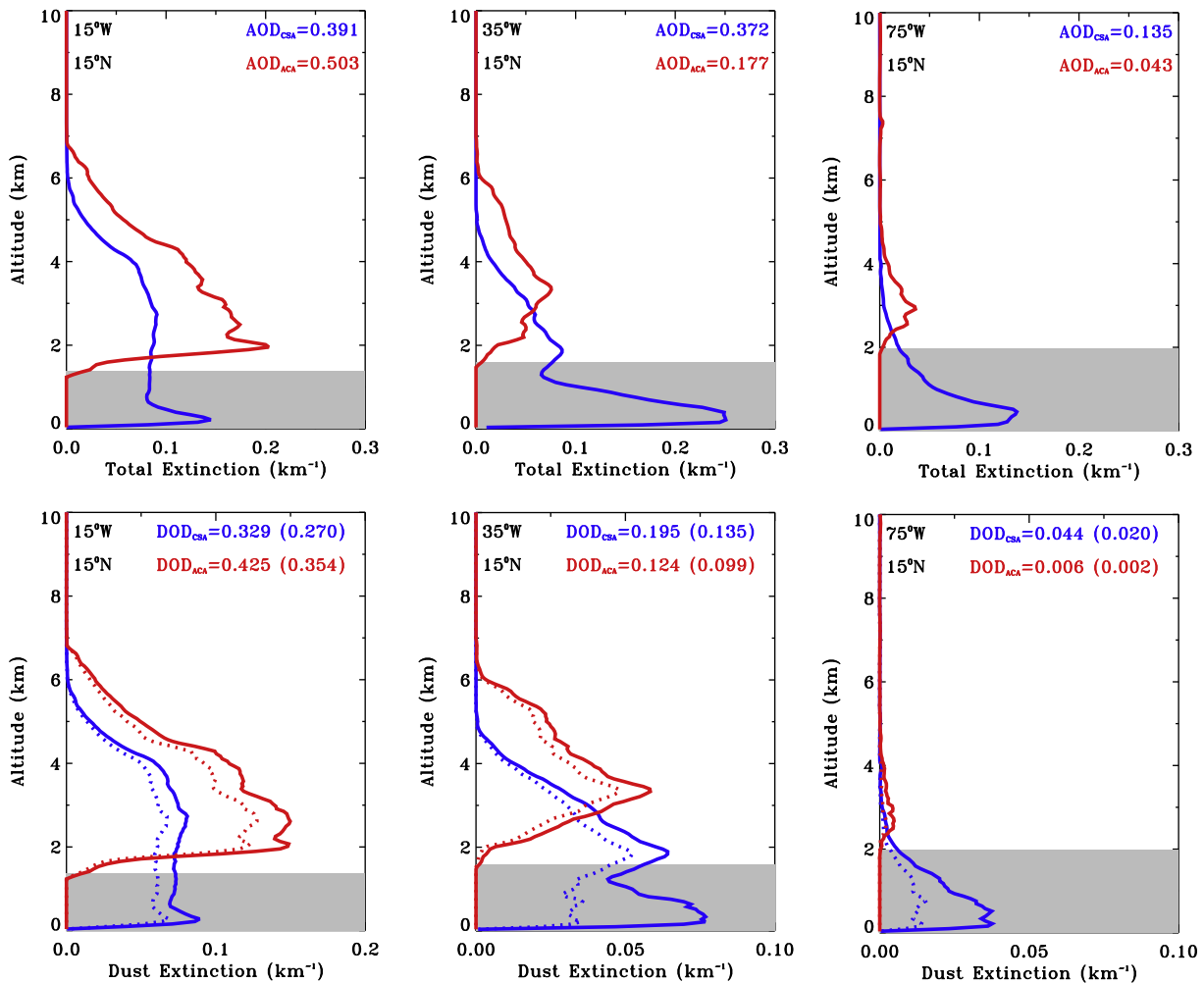


Fig. 5. Vertical profiles of $10^{\circ}N$ – $20^{\circ}N$ averaged total (top panels) and dust (bottom panels, solid line and dashed line for the UDF and LDF scenarios, respectively) extinction coefficient (km^{-1}) for CSA (blue) and ACA (red) at $15^{\circ}W$, $35^{\circ}W$, and $75^{\circ}W$ in MAM 2012. AOD and dust optical depth (DOD) in UDF (LDF) scenario are noted in the plots. The upper bound of shaded area marks the seasonal averaged top of low-level clouds.

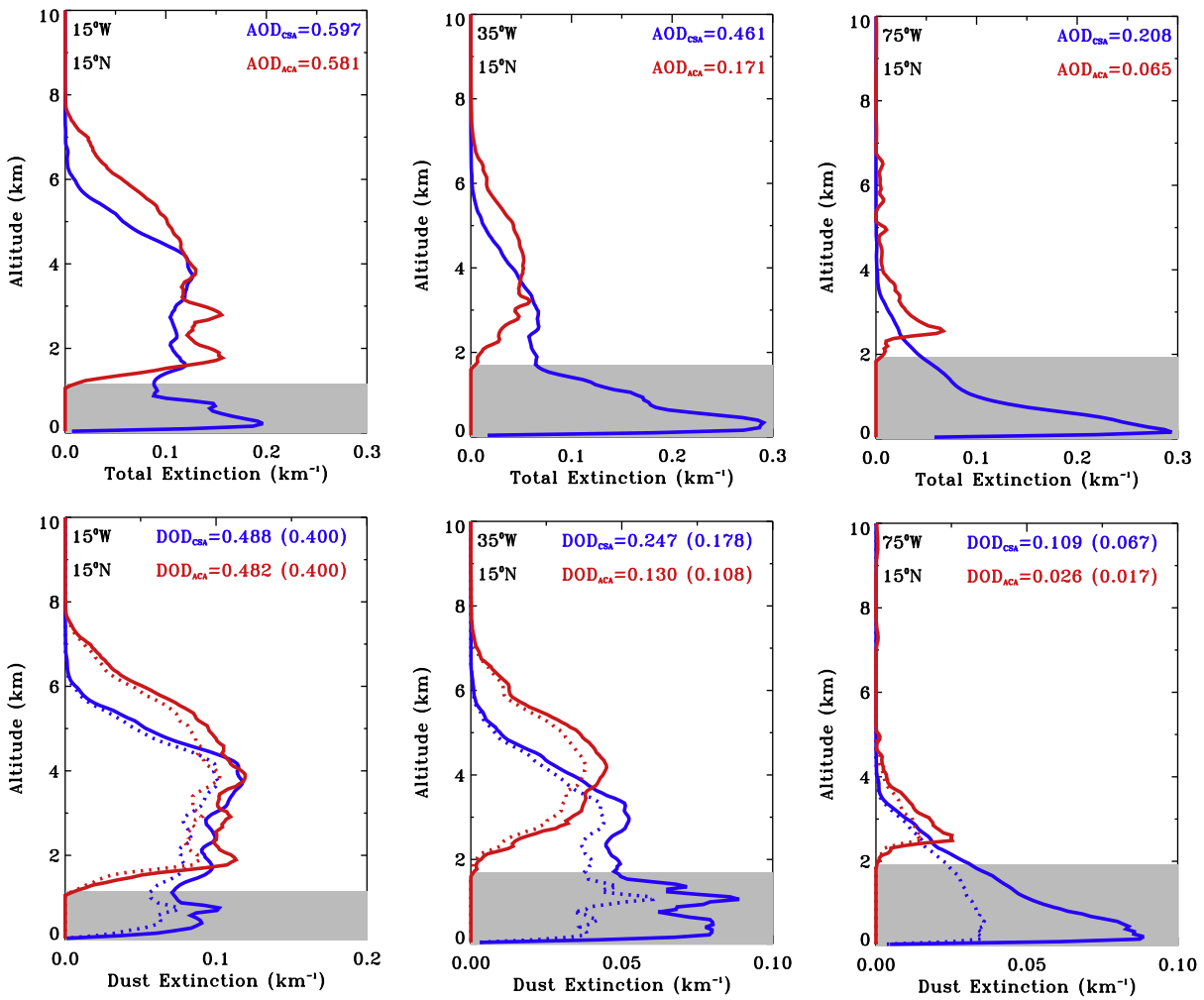


Fig. 6. Same as Fig. 5 except for JJA 2012.

An integration of the aerosol extinction coefficient in the vertical yields AOD. Fig. 7 shows the 2007–2013 average of total AOD for CSA and ACA in different latitude/longitude segments and seasons, with error bars indicating the standard deviation of AOD over the 7-year period. At all three longitudinal cross sections, the occurrence of peak AOD for both CSA and ACA shifts from 0° to 10°N in DJF and MAM to 10°N–20°N in JJA. In SON, while peak AOD occurs at 10°N–20°N latitudinal band at both 15°W and 35°W longitudinal cross sections, peak AOD occurs at 10°S–0°S at 75°W presumably because of the influence of biomass burning smoke transported from South America. In a majority of cases, AOD is greater for CSA than ACA, with the difference most pronounced at 35°W and 75°W. However the opposite could happen at 15°W.

While Fig. 7 shows the total AOD, Fig. 8 shows the separation of dust from non-dust AOD for CSA in the LDF scenario based on the 7-year average. We see clearly a northward shift of the major dust transport route when transitioning from DJF and MAM to JJA and SON. The fraction of dust AOD is higher in JJA and SON than in DJF and MAM. The dust fraction also decreases with increasing distance from the African continent. The dust fraction depends on the scenario used to separate dust from non-dust. As shown in Fig. 9, the DOD/AOD ratio for CSA is always higher in the UDF scenario than the LDF scenario. This generally holds true for ACA, except in a few occasions where the DOD/AOD ratio is more or less the same for the UDF and LDF scenarios.

How well do CALIOP AOD retrievals represent the seasonal and interannual trends over the Atlantic basin? To evaluate the CALIOP

retrievals in our area of interest, we compare with ground-based AOD observations. Fig. 10 compares CALIOP seasonal and regional averaged AOD for CSA with AERONET measurements near the coast of North Africa (Cape Verde, 16°N and 22°W) and in the Caribbean Sea (La Parguera, 17°N and 67°W). Some seasonal mean AODs from AERONET sites are missing, including 2011 SON at Cape Verde, 2010 JJA and SON as well as 2012 SON at La Parguera. Note that we are not doing simultaneous and collocated comparisons between CALIOP and AERONET like that in the literature (e.g., Omar et al., 2013; Schuster et al., 2012). Those rigorous comparisons found that CALIOP tends to underestimate AOD by about 30% in dusty regions. Here we focus mainly on the consistency in seasonal and interannual variations of AOD and its west–east gradient between CALIOP and AERONET. We found that in both sites, CALIOP and AERONET AOD have a linear correlation coefficient of 0.86, suggesting that CALIOP generally well-captured the seasonal variations of AOD observed by AERONET. Both sites exhibit profound seasonal variations of AOD by a magnitude of a factor of 2 to 5, with the highest values in JJA. However, AERONET usually reports the lowest AOD in DJF over both sites, whereas CALIOP persistently shows a minimum in SON at La Parguera. Overall, the seasonal AOD averaged over seven years from CALIOP agrees with AERONET within 27% at both sites, except in SON over La Parguera when AOD from CALIOP is 35% lower than that from AERONET. The largest difference between CALIOP and AERONET AOD is seen in 2011, when CALIOP at Cape Verde is 0.08–0.12 higher than AERONET in MAM and JJA but ~0.07 lower at La

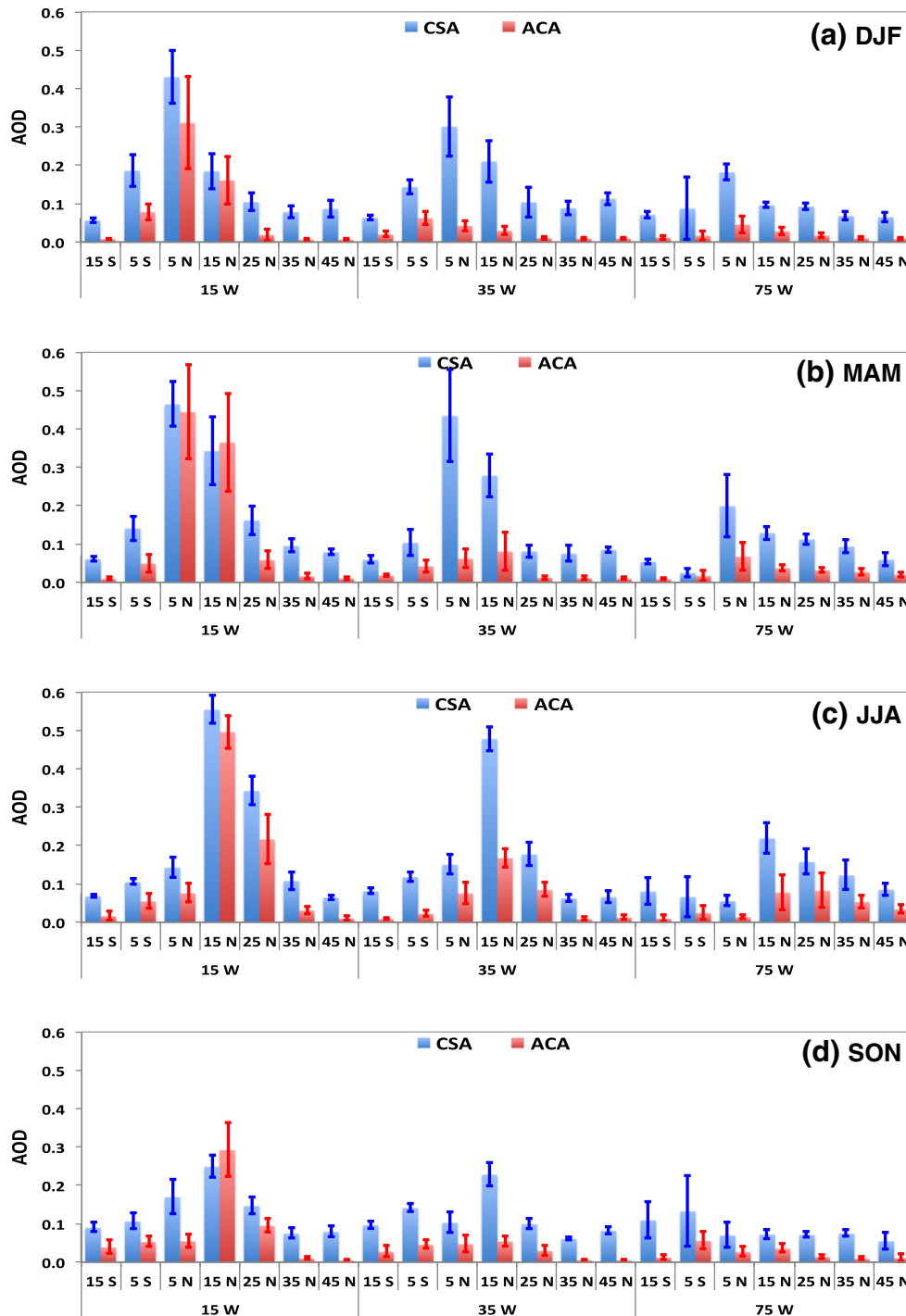


Fig. 7. Seven-year average AOD in individual $10^\circ \times 10^\circ$ segments (with central latitude and longitude labeled) for CSA (blue) and ACA (red) in different seasons: (a) DJF, (b) MAM, (c) JJA, and (d) SON. The error bar indicates standard deviation of AOD over the 7-year period.

Parguera in JJA and SON. Factors that contribute to this discrepancy may include heterogeneity in aerosol spatial distribution, and uncertainties in retrieval processes and instrument calibrations. Also shown in Fig. 10 is CALIOP-derived dust optical depth (DOD) with LDF and UDF scenarios. Although they generally follow the seasonal variation of the CALIOP AOD, at La Parguera the minimum DOD is shifted to DJF in most years (later than the AOD minimum season of SON) and at Cape Verde the peak DOD in 2010 appears in MAM (earlier than the AOD peak in JJA).

The AERONET data base also constrains the magnitude of the decrease in the AOD as dust transports across the Atlantic. We calculated the west to east AOD gradient as a ratio of La Parguera to Cape Verde for AERONET and 75°W to 15°W for CALIOP. The AERONET west-to-east gradient is 0.36, 0.46, 0.53, and 0.34 in DJF, MAM, JJA, and SON, respectively. The corresponding CALIOP-based gradient is 0.56, 0.42, 0.39, and 0.31, respectively. Even though CALIOP and AERONET agree on the values in MAM and SON, they have different seasonal variations of the AOD ratios: AERONET shows the weakest west-to-east gradient in JJA

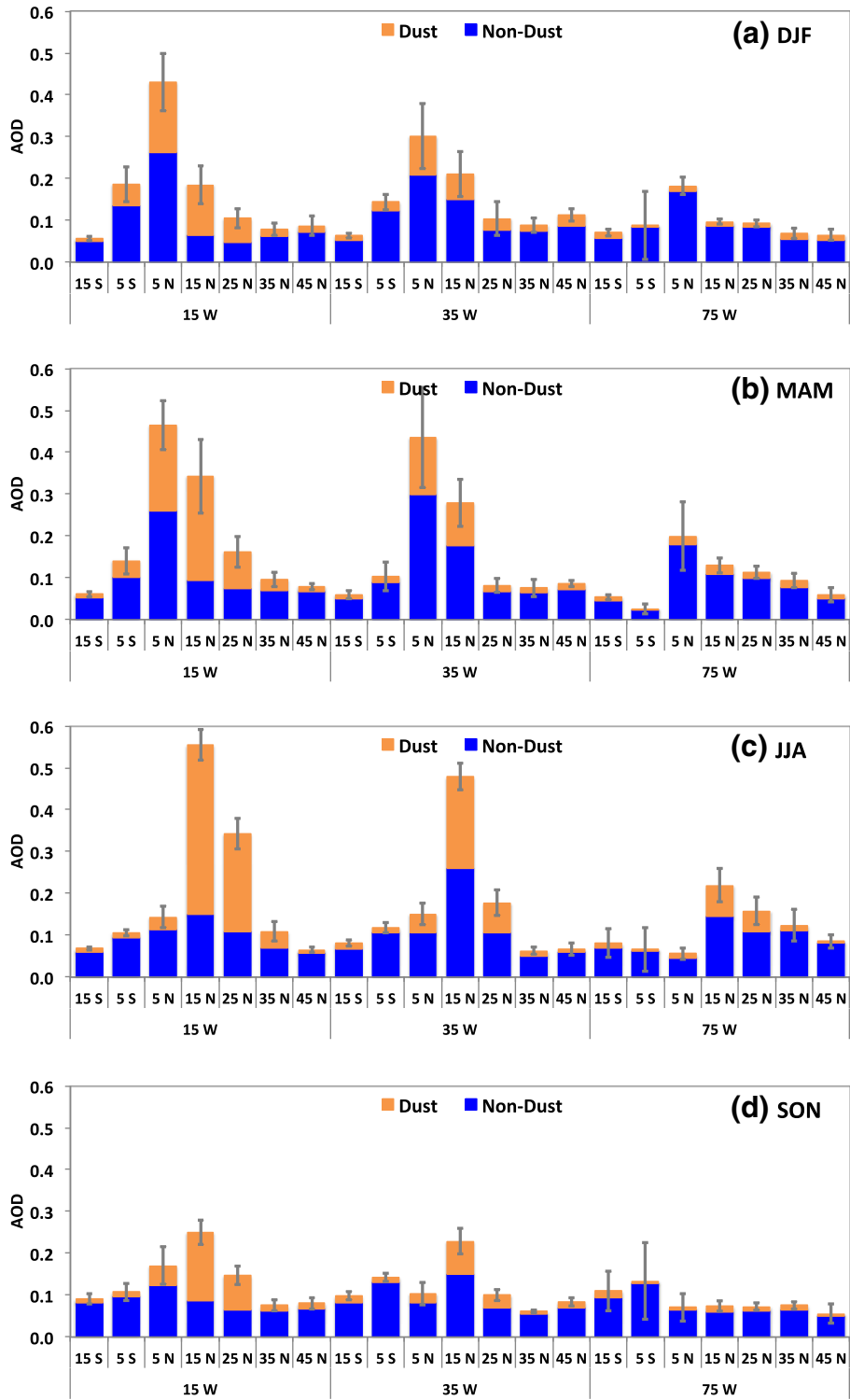


Fig. 8. Seven-year average AOD in each segment for CSA in the LDF scenario in different seasons: (a) DJF, (b) MAM, (c) JJA, and (d) SON. AOD is partitioned into dust (orange) and non-dust (blue) aerosol. Gray error bar indicates standard deviation of total AOD over the 7-year period.

(indicated by the largest AOD ratio of 0.53) but CALIOP indicates that in DJF (with the largest AOD ratio of 0.56).

3.2. Trans-Atlantic dust mass flux from CALIOP

Given that the statistics of the CALIOP AOD, which is integrated extinction, resembles the seasonal, interannual and gradients of the

AERONET ground-truth, we translate the optical measurements and retrievals to estimates of mass and mass flux. With the dust extinction profiles derived in 3.1, we calculate the dust mass flux by converting dust extinction coefficient to dust mass concentration with the assumed MEE of $0.37 \text{ m}^2 \text{ g}^{-1}$. Then the dust mass flux is calculated using MERRA zonal wind profiles (Eqs. 2–4). Fig. 11 shows seasonal, interannual, and meridional variations of CALIOP dust mass fluxes during the cross-ocean

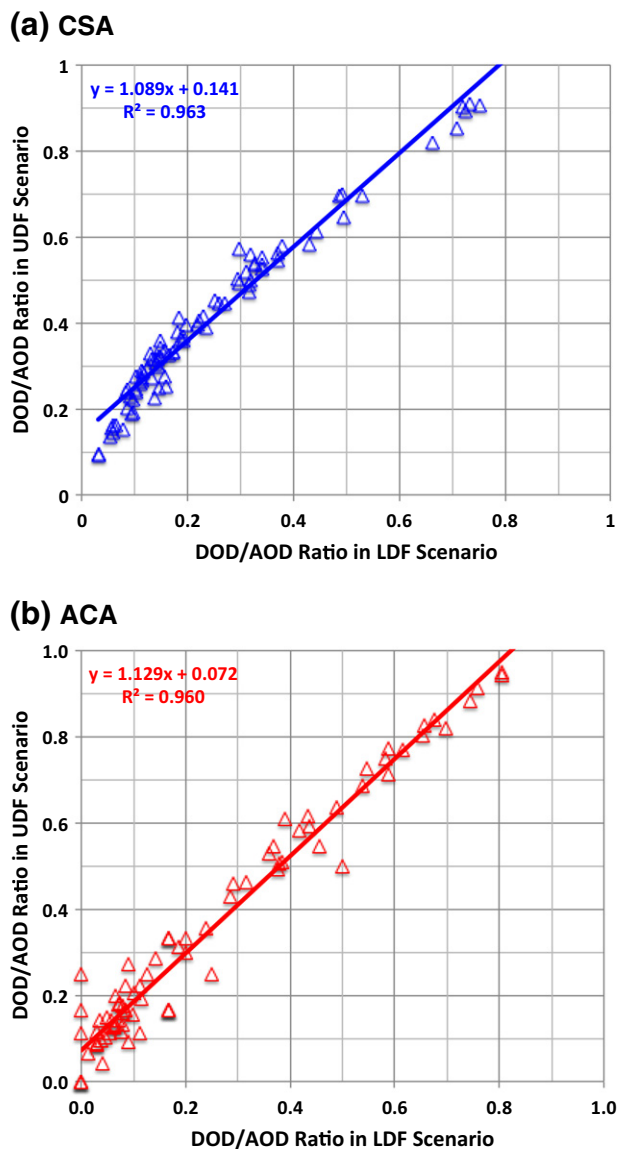


Fig. 9. Correlation of dust fraction (DOD/AOD ratio) between UDF scenario and LDF scenario for (a) CSA and (b) ACA. Each data point represents a 7-year average in a season and over a $10^\circ \times 10^\circ$ box. A total of 21 boxes are considered, with 7 boxes (between 20°S – 50°N) each of three longitudinal cross sections centered at 15°W , 35°W , and 75°W , respectively. Thus each plot has a total of 84 data points. A linear regression line and equation are inserted.

transport in the LDF scenario. Table 1 lists corresponding annual dust flux and percentage contribution from different seasons, with both 7-year average and range (in parentheses) shown. Clearly the dust mass flux integrated over the 10°S – 30°N latitude strip has a maximum in JJA and a minimum in SON. On a basis of a 7-year average, the percentage contribution for JJA is 46, 38, and 61% at the cross section of 15°W , 35°W , and 75°W , respectively. The percentage contribution from SON is 10–12%. The relative contribution for DJF and MAM differs by the cross section. On a basis of the 7-year average, DJF and MAM make similar contributions at 15°W , whereas the MAM contribution is higher than the DJF contribution at 35°W and 75°W . The dust mass flux shows significant interannual variations in terms of both the magnitude of annual flux and seasonal contributions. The year-to-year variation is up to 86%. The annual dust fluxes are smallest in 2011, because of the smallest dust AOD as discussed earlier (see Fig. 10). However the largest dust flux occurred in 2007 at 15°W and 35°W , but in

2012 at 75°W . Also notable from Fig. 11 is that in 2010 dust mass flux in MAM is much higher than that in DJF, which differs from other years.

On an annual basis, Fig. 11(d)–(f) (right panels) show that major trans-Atlantic transport occurs in the 0° – 20°N latitude strip, with the largest flux in the 10°N – 20°N strip. Dust flux also shows a meridional drift over a year, which is mainly determined by the advance and retreat of the intertropical convergence zone (ITCZ). At 15°W and 35°W , the dust transport occurs predominantly in 10°N – 20°N in JJA, but shifts southward to 0° – 10°N in MAM and DJF when the ITCZ moves to the South. At 75°W , the dust flux is more or less evenly distributed in the 0° – 10°N and 10°N – 20°N strips in DJF and MAM, but it moves dramatically northward into the 10°N – 20°N strip, bleeding over into the 20° – 30°N strip in JJA.

In the UDF scenario, a larger fraction of aerosol extinction is partitioned into dust than that in the LDF scenario. While the magnitude of dust extinction is higher in the UDF scenario, no significant difference is observed for the shape of the dust vertical profile in the UDF and LDF scenarios (c.f., Figs. 5 and 6). Thus the estimated dust mass fluxes are larger for the UDF scenario (F_{UDF}) than for the LDF scenario (F_{LDF}), as shown in Table 2. We calculate an average flux of LDF and UDF scenarios (F_{ave}) and use it as the best estimate of dust mass flux. On the basis of a 7-year average, the best estimate of annual dust mass flux is 182.2, 131.8, and 43.1 Tg a^{-1} at the cross section of 15°W , 35°W , and 75°W , respectively. We also calculate a ratio of $(F_{\text{UDF}} - F_{\text{LDF}}) / (F_{\text{UDF}} + F_{\text{LDF}})$ to represent relative uncertainty (RU) associated with the dust and non-dust separation scheme. As shown in Table 2, the 7-year average RU increases from 14.6% at 15°W to 24.2% at 35°W and to 33.8% at 75°W . RU has no significant interannual variation. This clearly shows that the method to distinguish dust from non-dust aerosol in this study is more sensitive to the thresholds of depolarization ratio in remote regions than near-source regions. Because of deposition, settling, and scavenging of dust along the cross-ocean transport route, the fraction of dust in dust-marine aerosol mixtures and hence the observed aerosol depolarization ratio decreases. When lowering the threshold values of characteristic depolarization ratio in the UDF scenario, there is a larger possibility that more extinction profiles are categorized into dust in the western Atlantic than in the eastern Atlantic.

Because CALIOP reports dust vertical profiles, we can calculate the vertical distribution of dust mass flux, which could not be done by using MODIS measurements (Kaufman et al., 2005). Fig. 12 shows the vertical profile of the 7-year mean dust mass flux with seasonal distinction for an average of the LDF and UDF scenarios. In the figure, dust mass fluxes in four seasons (marked with different colors) are accumulated so that the rightmost profiles show the vertical distribution of annual dust mass fluxes. The figure shows that the relative contributions of dust mass flux from different seasons change with altitude. At 15°W and 35°W , the annual dust mass flux is dominated by contributions from DJF and MAM at altitudes lower than 2–3 km; and the lower the altitude, the higher the DJF contribution. At higher altitudes, the annual dust mass flux is predominated by the dust transport in JJA. The dust mass flux above 4 km comes exclusively from JJA. At 75°W , the dust mass flux is consistently higher in JJA than in other seasons at all altitudes. There is a flux spike around 4 km at 75°W , which comes largely from several high-altitude transport events detected by CALIOP. For example, the flux rate of greater than 1 Tg km^{-1} occurred in SON of 2007, DJF of 2008, MAM of 2010, JJA of 2011, DJF of 2012, and DJF, JJA, and SON of 2013.

The interannual variation of African dust and trans-Atlantic transport has been related in previous studies (Chiapello & Moulin, 2002; Chiapello et al., 2005; Chin et al., 2014; Ginoux, Prospero, Torres, & Chin, 2004; Moulin et al., 1997; Prospero & Lamb, 2003) to some climate indices, such as the North Atlantic Oscillation (NAO) index (Hurrell, 1995) and the Sahel Precipitation Index (SPI) (Janowiak, 1988). Here we examine correlations between the CALIOP dust mass flux and these climate indices. Fig. 13 shows interannual variations of wintertime (DJF) CALIOP dust mass flux (in the LDF scenario) and the principal

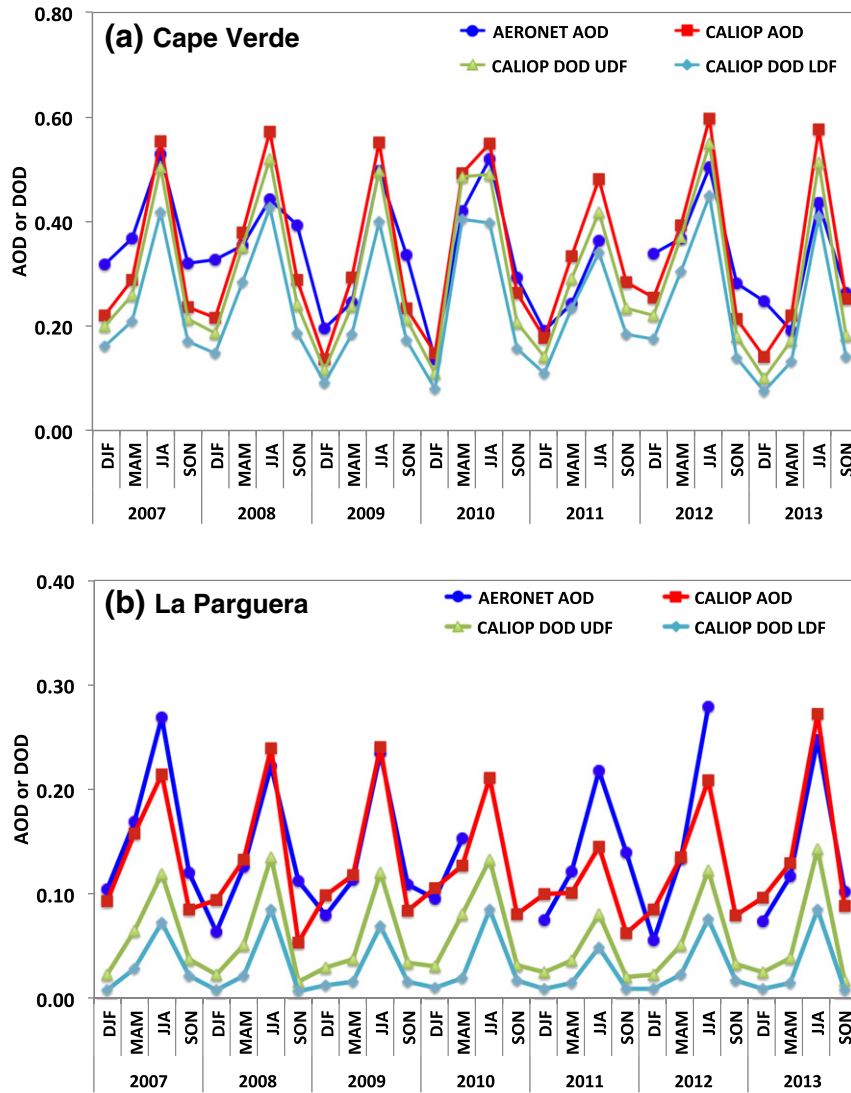


Fig. 10. Comparisons of seasonal and interannual variations of AOD between AERONET (blue) and CALIOP (red) at (a) Cape Verde (16°N, 22°W) and (b) La Parguera (17°N, 67°W). DOD estimated from CALIOP is also shown, with cyan for LDF and green for UDF scenario. CALIOP values are averages over the 10° × 10° box centered at (15°N, 15°W) for Cape Verde and (15°N, 75°W) for La Parguera, respectively. Note that some seasonal mean AODs from AERONET are missing, including 2011 SON at Cape Verde, 2010 JJA and SON as well as 2012 SON at La Parguera. In both sites, CALIOP and AERONET AOD have a linear correlation coefficient of about 0.87. Based on a 7-year average, the AOD bias (CALIOP/AERONET) at Cape Verde is 0.77, 1.12, 1.19, and 0.87 in DJF, MAM, JJA, and SON, respectively. Corresponding AOD biases at La Parguera are 1.27, 0.97, 0.90, and 0.65.

component (PC)-based NAO index in DJF (<https://climatedataguide.ucar.edu/climate-data/hurrell-north-atlantic-oscillation-nao-index-pc-based>, accessed 01 August 2014). Clearly, the wintertime dust mass flux follows the interannual variation of NAO index well. The larger the DJF NAO index, the larger the dust mass fluxes are. The linear correlation coefficient (R) is calculated as 0.80, 0.83, and 0.70 at 15°W, 35°W, and 75°W, respectively. The former two correlations are tested as statistically significant at the 95% confidence level. For other seasons, we do not see clear correlation of dust mass flux with the NAO index. Our results are consistent with that of previous studies showing dominant influence of NAO during the winter season and in regions not remote to the sources (Chiapello et al., 2005; Ginoux et al., 2004; Moulin et al., 1997).

Similarly we examine possible relationship between CALIOP annual dust mass flux and the prior-year SPI averaged over June–October (i.e., the rainfall season of 10°–20°N, 20°W–10°E) [<http://jisao.washington.edu/data/sahel/>; doi:10.6059/H5MW2F2Q], as shown in Fig. 14. Clearly the estimated annual dust mass fluxes are highly anti-correlated with the prior-year SPI, with R² of 0.59 to 0.86 (all

correlations are statistically significant at the 95% confidence level), which is consistent with previous studies (Chiapello et al., 2005; Prospero & Lamb, 2003). We also found that the SPI and annual NAO index are well anti-correlated with a correlation coefficient R of –0.82 over the period of this study (2007–2013). Thus the dust mass flux is also positively correlated with the prior-year NAO index but with smaller correlation coefficients, with R² of 0.50, 0.24, and 0.79 at 15°W, 35°W, and 75°W, respectively. On a seasonal basis, the dust mass fluxes in DJF, MAM, and JJA are also anti-correlated with the prior-year SPI but positively correlated with the prior-year NAO, as shown in Table 3. In some seasons and locations, the correlation is statistically significant at the 95% confidence level. On the other hand, the dust mass flux in SON has no consistent anti-correlation or correlation with the climate indices.

Finally, we investigate a possible link between the satellite-derived dust mass fluxes and surface dust concentrations measured at an island site. Surface dust concentration has been measured at Barbados (13.17°N, 59.53°W) since 1965 by the University of Miami (Prospero, 1999; Prospero & Lamb, 2003). This longest dust record has been used extensively to understand the transport and impacts of African dust on the

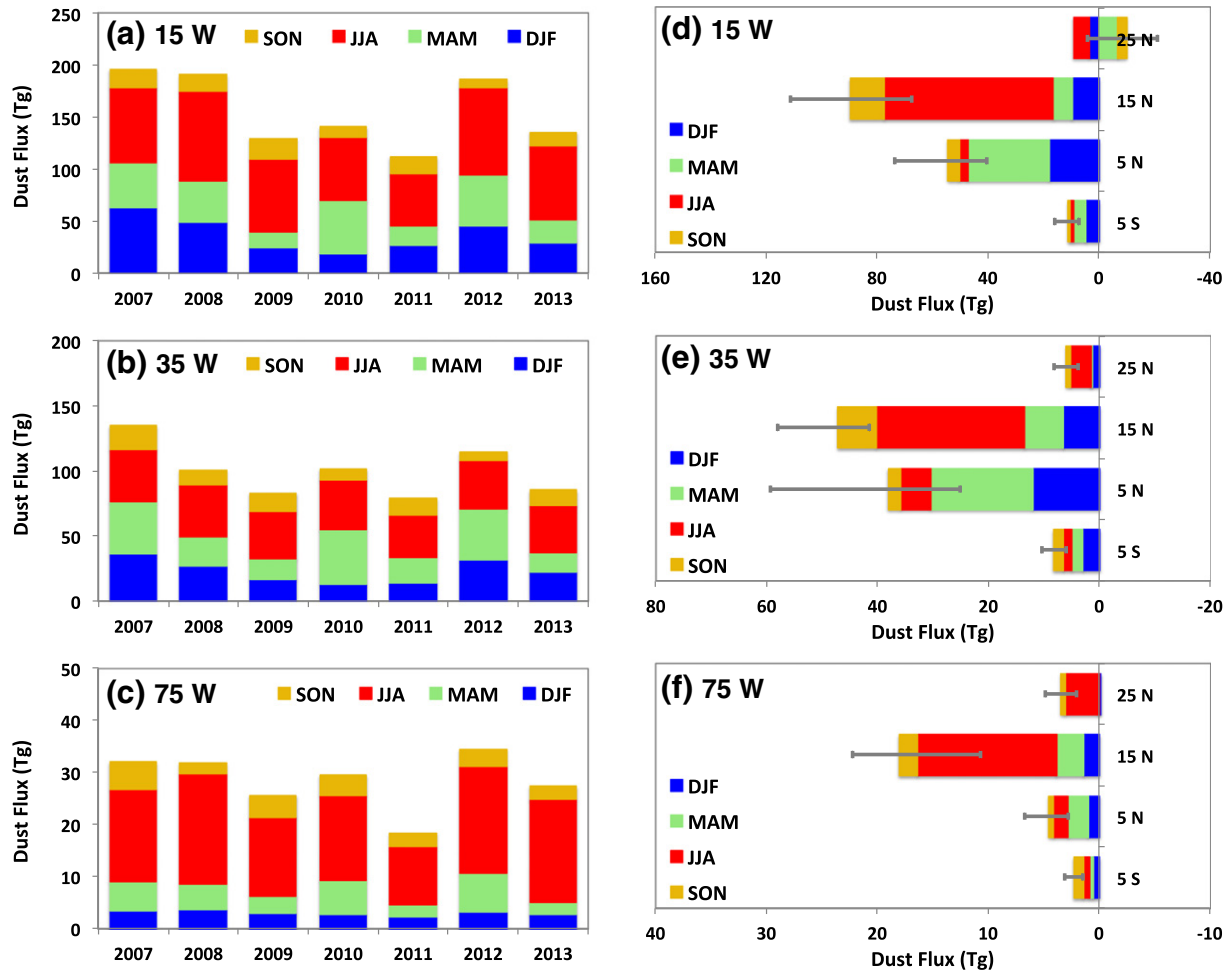


Fig. 11. Dust mass flux (Tg) integrated over 10°S–30°N (left panels) and its meridional distribution (right panels) at the cross section of (a, d) 15°W, (b, e) 35°W, and (c, f) 75°W derived from CALIOP observations for the LDF scenario. Seasonal distinction is reflected by the color of the stacked bar. In the right panels, a stacked bar represents the 7-year mean dust flux, while the error bar indicates the range of annual flux over the 7 years.

Caribbean Sea (e.g., Chiappello et al., 2005; Chin et al., 2014; Prospero & Lamb, 2003; Prospero et al., 2005, 2014). Fig. 15 shows a comparative analysis of seasonal mean dust concentration ($\mu\text{g m}^{-3}$) near the surface of Barbados and CALIOP dust mass flux (Tg per season) in the LDF and UDF scenarios from 2007 to 2011 (Barbados dust measurements after 2011 were not available when this study was performed). The CALIOP dust mass flux was calculated upwind of Barbados at the cross section of 50°W and integrated over the 8°N–18°N segment. A major difference shown in Fig. 15(a) is that while surface dust concentrations in MAM and JJA 2010 were among the highest over the 5-year period, CALIOP estimated dust flux has the highest value in JJA 2007. Overall the CALIOP estimated dust mass flux upwind of Barbados shows a linear correlation with the surface dust concentration on a seasonal basis, with R^2 of 0.66 and 0.70 for the LDF and UDF scenarios, respectively (Fig. 15(b)).

Table 1

The 7-year average of annual dust mass flux (Tg) in the zonal direction integrated over the 10°S–30°N latitudinal strip and seasonal contributions (%) derived from the CALIOP LDF scenario. Numbers in parentheses represent the range over the 7-year period.

Cross section	Annual flux (Tg)	Seasonal contribution (%)			
		DJF	MAM	JJA	SON
15°W	156 (112–196)	23 (13–32)	21 (12–36)	46 (37–55)	10 (4–15)
35°W	100 (79–135)	23 (13–27)	27 (17–41)	38 (30–43)	12 (6–18)
75°W	29 (19–35)	11 (9–13)	16 (9–22)	61 (55–72)	12 (7–16)

3.3. Comparisons of CALIOP and MODIS estimates of dust mass flux

How are the CALIOP-based dust flux estimates compared with the MODIS estimate as given in Kaufman et al. (2005)? Table 4 compares the CALIOP-based estimates of integrated dust mass flux over 10°S–30°N and the dust transport efficiency with that from the MODIS estimate (Kaufman et al., 2005). At 15°W and 75°W cross sections, the MODIS-based dust flux is within the range of the CALIOP–UDF estimate but significantly higher than the CALIOP–LDF estimate. At the cross section of 35°W, the MODIS estimate falls in between the CALIOP–LDF and CALIOP–UDF estimates. Because of the large interannual variation of dust mass flux, CALIOP–MODIS comparisons need to factor in the interannual variations. As shown earlier (e.g., Fig. 14), the dust mass fluxes are anti-correlated with the prior-year SPI. We found that SPI for 2000 ($-1.25 \text{ cm month}^{-1}$) is comparable to that of 2006 ($-0.9 \text{ cm month}^{-1}$) and 2007 ($-1.29 \text{ cm month}^{-1}$). It is anticipated that the dust mass flux for 2001 would be comparable to the estimates for 2007 and 2008, the upper bound of the 7-year CALIOP estimates. If such interannual variation is taken into account, the MODIS dust flux agrees well with CALIOP LDF estimate at 15°W and 35°W, but with CALIOP UDF estimate at 75°W. Table 4 also gives the comparison between the CALIOP and MODIS-based dust transport efficiencies, which is defined in the eastern tropical Atlantic as the ratio of the 10°S–30°N integrated seasonal dust mass flux (in the zonal direction) at 35°W to that at 15°W; and defined in the western tropical Atlantic as the seasonal flux ratio between 75°W

Table 2

Comparison of CALIOP annual dust mass flux (Tg) integrated over the 10°S–30°N latitudinal strip for the LDF scenario (F_{LDF}), UDF scenario (F_{UDF}), and an average of LDF and UDF flux (F_{AVE}) at the three longitudinal cross sections. The relative uncertainty (RU) is calculated as $(F_{UDF} - F_{LDF}) / (F_{UDF} + F_{LDF})$, which is considered to be a measure of uncertainty associated with the dust and non-dust separation scheme used in this study.

Cross-section	Flux or RU	2007	2008	2009	2010	2011	2012	2013	2007–2013 average
15°W	F_{LDF} (Tg)	195.9	190.7	129.3	140.5	111.5	185.9	135.5	155.6
	F_{UDF} (Tg)	257.3	252.6	176.4	192.1	153.9	243.9	185.2	208.8
	F_{AVE} (Tg)	226.6	221.7	152.9	166.3	132.7	214.9	160.4	182.2
	RU (%)	13.5	14.0	15.4	15.5	16.0	13.5	15.5	14.6
35°W	F_{LDF} (Tg)	134.8	100.8	83.4	101.8	78.8	114.8	85.3	99.9
	F_{UDF} (Tg)	215.5	164.4	141.3	161.0	132.2	188.3	142.3	163.6
	F_{AVE} (Tg)	175.2	132.6	112.4	131.4	105.5	151.6	113.8	131.8
	RU (%)	23.0	24.0	25.8	22.5	25.3	24.2	25.0	24.2
75°W	F_{LDF} (Tg)	32.1	31.9	25.7	29.6	18.5	34.5	29.9	28.5
	F_{UDF} (Tg)	64.9	63.1	55.2	59.5	38.3	67.4	54.5	57.6
	F_{AVE} (Tg)	48.5	47.5	40.5	44.6	28.4	51.0	42.2	43.1
	RU (%)	33.8	32.8	36.5	33.6	34.9	32.3	29.1	33.8

and 35°W. Thus the transport efficiency measures the rate of dust loss during the transport via dry and wet removal and the meridional transport. The smaller the transport efficiency, the more the loss of dust is. As shown in Table 4, in the eastern tropical Atlantic (15°W–35°W), the MODIS dust transport efficiency of 0.54 is lower than the CALIOP estimates of 0.68 and 0.83 for the LDF and UDF scenarios, respectively. In the western tropical Atlantic (35°W–75°W), on the other hand, the MODIS estimate of 0.46 is higher than the CALIOP estimates of 0.28 and 0.35 for the LDF and UDF scenarios, respectively. For the whole tropical Atlantic, the MODIS-based transport efficiency of 0.25 falls within the range of the CALIOP–LDF and CALIOP–UDF estimates.

Larger CALIOP–MODIS differences exist in the meridional distribution of the dust mass flux, as shown in Fig. 16. Near the source region (at 15°W), the MODIS flux shows a factor of 3 difference between the 10°–20°N and 0°–10°N strip. Such difference is reduced to 30–50% for the CALIOP flux. The MODIS flux is close to the largest CALIOP flux in the UDF scenario in 10°–20°N, while in 0°–10°N the MODIS flux is close to the 7-year average of CALIOP flux in the LDF scenario. At 35°W, the MODIS flux falls in between the CALIOP LDF and UDF estimates, and is closer to the CALIOP LDF estimate. In the further remote regions (at 75°W), in both 10°–20°N and 0°–10°N the MODIS flux is close to the highest CALIOP flux among the 7 years in the UDF scenario. Kaufman et al. (2005) estimated that the net zonal dust flux of 50 Tg in the region of (20°S–10°N, 35°W–75°W), which has been used as an approximate for the dust deposition into the Amazon Basin. In comparison, the CALIOP corresponding estimate ranges from 40 (for the LDF

scenario) to 66 Tg a⁻¹ (for the UDF scenario). This suggests that the MODIS estimate agrees well with the CALIOP estimates. However, we caution that using such estimated net zonal dust flux to represent the dust deposition in the Amazon Basin may complicate comparisons between measurements and measurements, and between measurements and model simulations (e.g., Bristow, Hudson-Edwards, & Chappell, 2010; Kaufman et al., 2005; Ridley et al., 2012). Careful attention should be exercised when interpreting the documented discrepancies in the literature and discussing their important implications for the biogeochemical cycles in the Amazon. A separate paper will be devoted to focus on this issue in terms of potential contribution from meridional transport and geographical definition of the Amazon Basin.

4. Discussion

4.1. Contribution of above-cloud aerosol measurements

The CALIOP capability of detecting aerosols above the low-level clouds offers a possibility of evaluating uncertainty associated with the use of passive remote sensing of cloud-free aerosols to calculate aerosol mass fluxes as assumed in previous studies (Kaufman et al., 2005; Yu et al., 2008; Yu, Remer et al., 2012). Table 5 lists the 7-year average and range of clear-sky to all-sky ratio for the 10°S–30°N integrated seasonal dust mass flux (F_{CSA}/F_{ALL}). F_{ALL} is the weighted average of F_{CSA} and F_{ACA} with the respective fraction of sky condition (Eq. 4), assuming that aerosol below low-level clouds is zero in the ACA condition. It shows

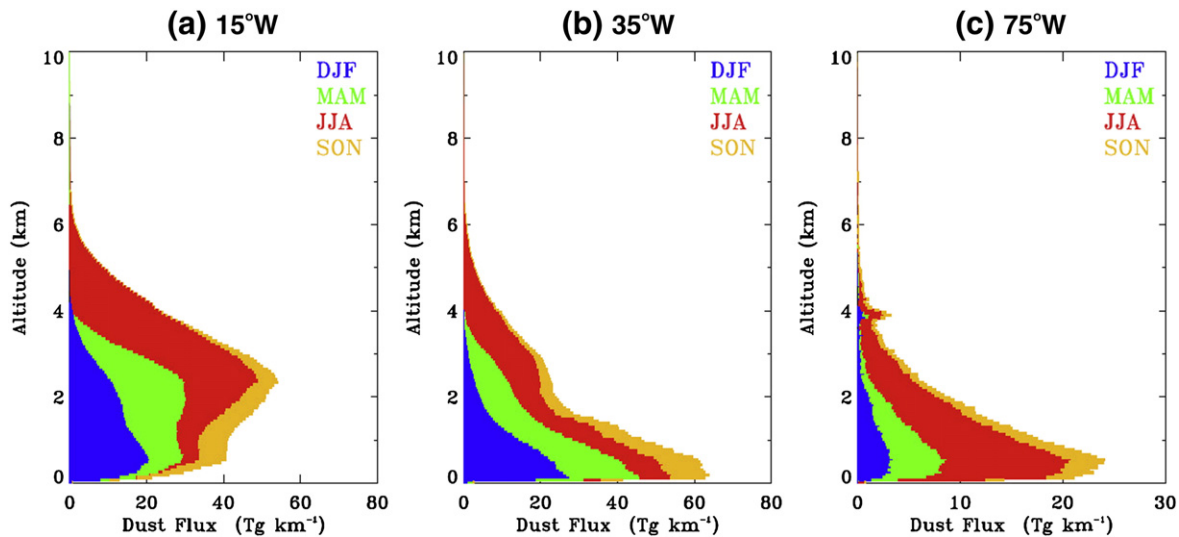


Fig. 12. The 7-year mean vertical profiles of annual dust flux (Tg km⁻¹) integrated over 10°S–30°N and averaged between LDF and UDF estimates at (a) 15°W, (b) 35°W, and (c) 75°W cross sections. Seasonal contributions are marked with different colors.

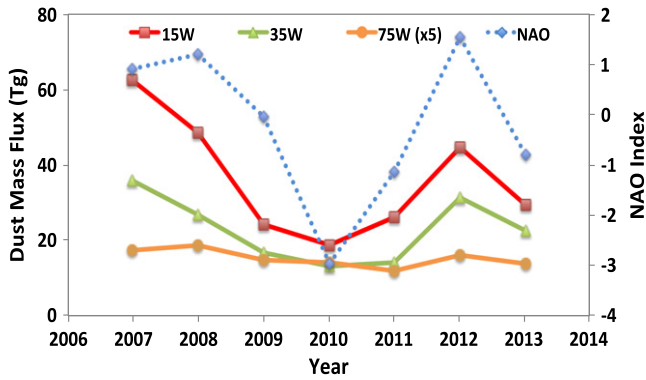


Fig. 13. Interannual variations of DJF NAO index and CALIOP 10°S–30°N integrated DJF dust mass flux at 15°W, 35°W, and 75°W in the LDF scenario, which shows that the wintertime dust mass flux is positively correlated with the DJF NAO index, with a correlation coefficient R of 0.80, 0.83, and 0.70 at 15°W, 35°W, and 75°W, respectively. The former two correlations are tested as statistically significant at the 95% confidence level, while the latter correlation is statistically significant at the 90% confidence level.

that the F_{CSA}/F_{ALL} depends on region, season, and year. At the cross section of 15°W, the ratio is generally close to 1. At the cross section of 35°W and 75°W, the F_{CSA}/F_{ALL} ratio is relatively large, particularly in DJF and MAM. On the basis of the 7-year average, the largest F_{CSA}/F_{ALL} ratio is 1.23 in DJF, suggesting a high bias of 23% in the estimated dust mass flux resulting from the use of clear-sky aerosol measurements only. In one particular year (2009), the high bias can be as much as 42%.

In the above estimates CALIOP nighttime CSA and ACA fraction (f_{CSA} and f_{ACA} , respectively) are used, which neglects possible diurnal variations of clouds in the region. A full characterization of such diurnal variations requires measurements from geostationary satellites, which is beyond the scope of this study. Nevertheless we examine the sensitivity of F_{CSA}/F_{ALL} ratio to f_{ACA} by halving and doubling the value of f_{ACA} (when doubling f_{ACA} is greater than 1, it is set at 1). As shown in Fig. 17 for the relative difference of flux DF ($DF = \frac{F_{CSA} - F_{ALL}}{F_{ALL}} \times 100\%$), doubling f_{ACA} yields a substantial increase of DF in DJF and MAM at the cross section of 35°W and 75°W, with the 7-year average DF of 42–62%. We thus anticipate that in the case of significant diurnal variations of f_{CSA} and f_{ACA} the use of cloud-free measurements could introduce significant uncertainties to the dust flux estimate. However, a caveat is that we do not have below-cloud aerosol measurements to give a more certain estimate

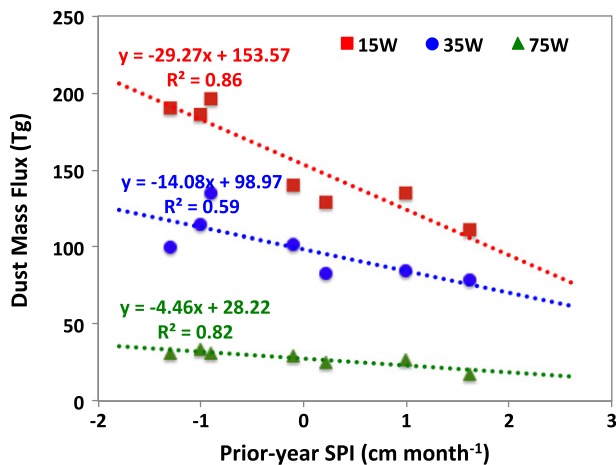


Fig. 14. Anti-correlation of CALIOP LDF 10°S–30°N integrated annual dust mass flux (Tg) at 15°W, 35°W, and 75°W with previous-year SPI (cm month^{-1}). The linear fit is shown as a dotted line with R^2 denoted (R is linear correlation coefficient). The correlations at 15°W and 75°W are tested as statistically significant at the 99% confidence level, while that at 35°W is statistically significant at the 95% confidence level.

Table 3

Correlation coefficient (R) of seasonal dust mass flux at 15°W, 35°W, and 75°W with prior-year SPI and NAO index. The bold number indicates that the correlation is statistically significant at a confidence level of 95%.

Climate index	Season	15°W	35°W	75°W
Prior-year SPI	DJF	-0.697	-0.702	-0.938
	MAM	-0.745	-0.587	-0.808
	JJA	-0.812	-0.904	-0.719
	SON	+0.169	+0.137	-0.245
Prior-year NAO	DJF	+0.428	+0.590	+0.779
	MAM	+0.480	+0.293	+0.614
	JJA	+0.899	+0.731	+0.856
	SON	-0.226	-0.241	+0.152

of bias associated with using clear-sky aerosols. Ground-based lidars can detect aerosols below low-level clouds, which may complement CALIOP in assessing cloudy-sky aerosol profiles in a full column. The above estimated clear-sky to all sky flux ratio or DF can be considered as an upper bound for the potential bias of using clear-sky aerosol measurements only.

4.2. Differences in dust fluxes between using daytime and nighttime observations

We have used CALIOP nighttime observations to calculate the dust mass flux, because of the high quality of the nighttime data. An implicit assumption is that a CALIOP-observed aerosol profile at night is a good representative of the daily average. In source regions the day-night contrasts in wind, turbulent mixing, and convection could lead to pronounced differences in dust AOD and vertical distribution. However we believe that in the transported regions the diurnal variation of dust loading and vertical profile would be insignificant. This assumption is at least partially corroborated by previous studies of examining the

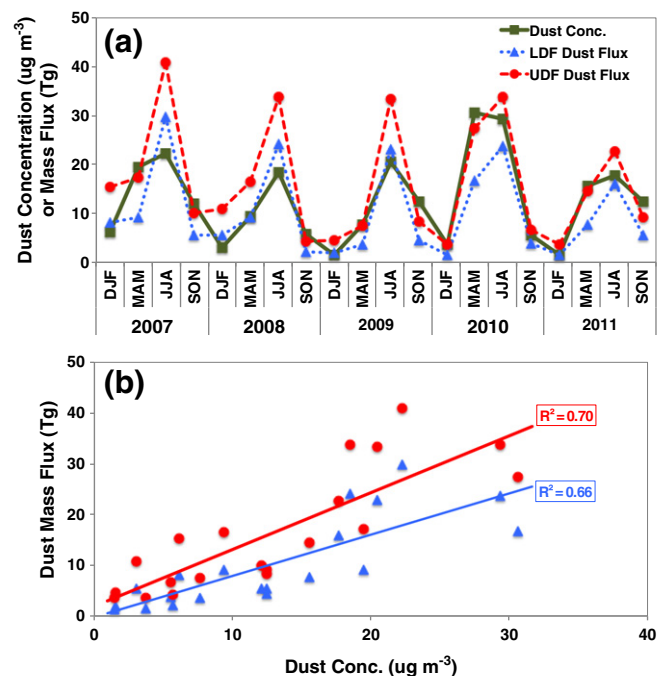


Fig. 15. (a) Comparison of surface dust concentration (green, $\mu\text{g m}^{-3}$) observed at Barbados (13°N , 60°W) with CALIOP estimated upwind seasonal-mean dust mass flux (Tg) in the LDF (blue) and UDF (red) scenarios; (b) correlation of CALIOP dust mass flux with surface dust concentration on a seasonal basis, with R^2 noted (R is linear correlation coefficient). The CALIOP dust mass flux upwind of Barbados was calculated at the longitudinal cross section of 50°W and integrated over the 8°N – 18°N segment.

Table 4

Comparison of annual dust mass flux integrated over the 10°S–30°N strip (unit: Tg) and dust transport efficiency (unitless, see text for definition) during the cross-Atlantic transport between CALIOP-based estimates (in the LDF and UDF scenarios) and MODIS-based estimate. The 7-year average is shown in bold, with the range listed in the parenthesis.

Method	10°S–30°N integrated flux (Tg)			Transport efficiency		
	15°W	35°W	75°W	35°W/15°W	75°W /35°W	75°W/15°W
CALIOP LDF	156 (103–214)	100 (76–136)	29 (17–37)	0.68 (0.55–0.76)	0.28 (0.23–0.31)	0.19 (0.17–0.22)
CALIOP UDF	209 (144–282)	164 (129–217)	58 (34–73)	0.83 (0.68–0.89)	0.35 (0.28–0.38)	0.29 (0.25–0.32)
MODIS	233	126	58	0.54	0.46	0.25

daytime variation of AOD. Smirnov et al. (2002) analyzed multiyear AERONET AOD measurements and found that the average variation from the daytime mean AOD is only about ±3% at Cape Verde, which is smaller than the ±10% over the source region (Ilorin, Nigeria). Zhang et al. (2012) did similar analysis at La Parguera and found that the average variation from the daytime mean AOD is within ±5%.

Diurnal variation of dust vertical profile and its influence on the dust mass flux estimate have not been assessed. Here we use CALIOP daytime and nighttime measurements in 2012 to perform a comparative analysis. The same dust and non-dust separation schemes and dust

flux calculations as described earlier are applied to CALIOP daytime and nighttime data. Fig. 18 shows a comparison of dust mass fluxes calculated with the daytime data with those using the nighttime data for 2012. The daytime-to-nighttime ratios of dust flux are listed in Table 6. Clearly the day–night difference in the dust mass flux depends on region and season. Near the African coast and in JJA, the dust mass flux estimated with the daytime data is 24% lower than the estimate with the nighttime data. In all other locations and seasons, the dust mass flux estimated from the daytime data is higher than that estimated from the nighttime data. Generally, the daytime-to-nighttime ratio is higher at locations far away from the source region than near the coast. On an annual average basis, the daytime-based dust flux is only about 4% lower than the nighttime-based dust flux at 15°W. On the other hand, the daytime-based dust flux is 53% and 71% higher than the nighttime-based estimate at 35°W and 75°W, respectively. However, we cannot attribute the examined differences shown here to meaningful physical processes, because of the difference in quality of CALIOP daytime and nighttime data. The CALIOP daytime data are subjected to larger uncertainties than the nighttime data (Winker et al., 2009). Because of the interference of sunlight, both aerosol extinction and depolarization measurements in daytime become more uncertain, which will affect the estimates of dust extinction and mass flux profiles.

4.3. Estimated uncertainties in the dust mass flux

The estimated dust mass fluxes are subjected to a range of uncertainties associated with the CALIOP observation itself and assumptions made in this study. Table 7 summarizes various sources of uncertainties, which are discussed in detail in the following.

It has been documented in rigorous (collocated and simultaneous sampling) validations against AERONET measurements that CALIOP daytime clear-sky measurements tend to underestimate AOD in the dusty regions by about 30% (e.g., Omar et al., 2013; Schuster et al., 2012). Most recently, Liu et al. (2014) compared CALIOP operational above-cloud AOD in nighttime with a more accurate retrieval using opaque water clouds as reference (Hu, 2007). They found that on a basis of a 6-year average, CALIOP operational above-cloud AOD in the dust outflow region was underestimated by ~26%, due primarily to the use of a too small dust lidar ratio and to a lesser degree to the mis-identification of the dust layer base. We assume that CALIOP nighttime AOD for both CSA and ACA in the region is underestimated by 30%. This low bias of DOD yields a 30% underestimate of dust mass flux. Although the magnitude of aerosol extinction coefficient or AOD can be biased high or low, the CALIOP observed shape of aerosol vertical profile is

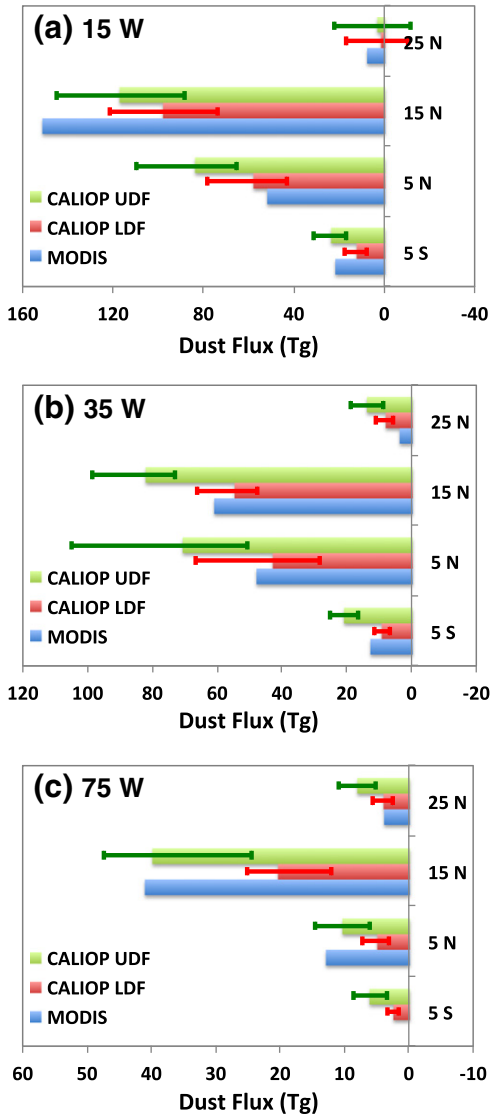


Fig. 16. Comparisons of annual dust mass flux (Tg) between the MODIS estimate (blue, taken from Kaufman et al., 2005) and CALIOP estimates under the LDF (red) and UDF (green) scenario (with wide-bar representing the 7-year average and error-bar denoting the range over the 7 years) at the cross-section of (a) 15°W, and (b) 35°W, and (c) 75°W.

Table 5

The 7-year average (the 7-year range in parentheses) of clear-sky (F_{CLR}) to all-sky (F_{ALL}) ratio for the 10°S–30°N integrated seasonal dust mass flux. F_{ALL} is the weighted average of F_{CLR} and F_{ACA} with the respective fraction (Eq. 4), assuming that aerosol below low-level clouds is zero in the ACA condition. These ratios are derived from the LDF scenario, but they are very similar in the UDF scenario.

Season	DJF	MAM	JJA	SON
15°W	1.05 (1.00–1.08)	0.99 (0.94–1.02)	0.98 (0.96–1.01)	1.12 (1.03–1.18)
35°W	1.23 (1.17–1.42)	1.20 (1.13–1.29)	1.14 (1.09–1.21)	1.10 (1.07–1.14)
75°W	1.22 (1.17–1.26)	1.18 (1.13–1.22)	1.06 (1.04–1.09)	1.12 (1.10–1.14)

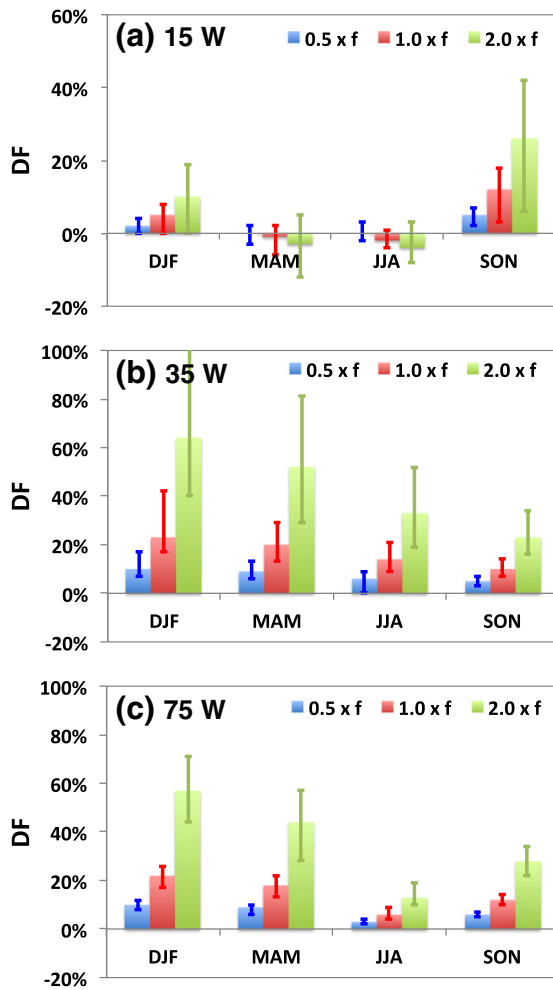


Fig. 17. Sensitivity of DF ($DF = \frac{F_{CSA} - F_{ALL}}{F_{ALL}} \times 100\%$) to ACA fraction (f) at the cross section of 15°W (a), 35°W (b), and 75°W (c), respectively. At 35°W , the upper bound of DF in DJF for the $2.0 \times f$ case (green error bar) is 142%, beyond the maximum of the y-axis.

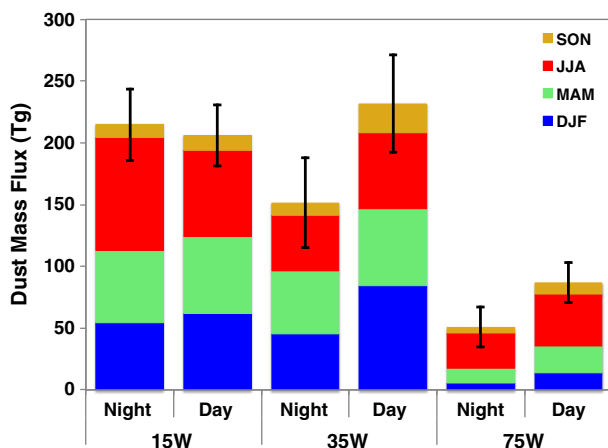


Fig. 18. Comparison of 10°S – 30°N integrated dust mass fluxes using CALIOP daytime (Day) and nighttime (Night) measurements for 2012. The stacked color bar shows the average of LDF and UDF estimated fluxes with seasonal distinction. The black error bar shows the range of annual dust mass flux in the LDF and UDF scenarios. It is important to note that the day-night difference in dust flux cannot be simply attributed to physical processes, because the daytime data are subjected to larger uncertainties than the nighttime data.

Table 6

Daytime-to-nighttime ratio for the dust mass flux (an average of estimates in the LDF and UDF scenarios) integrated over 10°S – 30°N in 2012.

Cross section	DJF	MAM	JJA	SON	Annual
15°W	1.14	1.07	0.76	1.17	0.96
35°W	1.86	1.23	1.35	2.38	1.53
75°W	2.59	1.83	1.46	1.86	1.71

fairly representative (Winker et al., 2009; Yu et al., 2010). Here we assume that uncertainty associated with the vertical profile is $\pm 10\%$ for the dust mass flux estimate.

Separating dust from non-dust aerosols with the depolarization measurement constitutes an important source of uncertainty in the estimated dust mass flux. As discussed earlier, we have used two sets of characteristic depolarization thresholds for dust and non-dust aerosols (denoted as LDF and UDF) to represent the lower- and upper-bound estimate of dust extinction and mass flux. If we take the average of LDF and UDF estimates as the best estimate of dust mass flux, the relative uncertainty associated with the dust and non-dust separation scheme is $\pm 15\%$, $\pm 24\%$, and $\pm 34\%$ at 15°W , 35°W , and 75°W , respectively, on a basis of the 2007–2013 average (see RU values in Table 2). Interannual variation of this type of uncertainty appears to be small.

In the estimate of dust mass flux, dust MEE of $0.37 \text{ m}^2 \text{ g}^{-1}$ is used to convert dust extinction coefficient at 532 nm to mass concentration, to be consistent with that used by Kaufman et al. (2005). This MEE value was selected based on observed particle size distributions with an assumption of dust density (Haywood et al., 2003; Maring, Savoie, Izaguirre, Custals, & Reid, 2003). While this value of MEE is consistent with an old database for transported dust in the free troposphere (Hess, Koepke, & Schult, 1998), it is smaller than some recent observations of Saharan dust. Chen et al. (2011) derived dust MEE of $1.1 \text{ m}^2 \text{ g}^{-1}$ based on airborne measurements of extinction and volume distribution for Saharan dust layers sampled largely over the Sahara Air Layer over the eastern North Atlantic Ocean. This estimate is biased high because of the low inlet sampling efficiency for particles greater than $4 \mu\text{m}$ (Chen et al., 2011). Ansmann et al. (2012) summarized several recent observation-based estimates of MEE for Saharan dust. Outside the source regions, the dust MEE falls into a range of 0.45 – $0.70 \text{ m}^2 \text{ g}^{-1}$, with an average of $0.53 \text{ m}^2 \text{ g}^{-1}$. The average MEE of $0.53 \text{ m}^2 \text{ g}^{-1}$ is greater than the $0.37 \text{ m}^2 \text{ g}^{-1}$ by 43%. For a given dust extinction, the dust mass is inversely proportional to MEE. Thus if the MEE of $0.53 \text{ m}^2 \text{ g}^{-1}$ is used for dust, the aforementioned dust mass flux will be reduced by 30%. This high bias of $\sim 30\%$ associated with dust MEE is largely compensated by the low bias resulting from AOD underestimate as discussed earlier.

During the trans-Atlantic transport, dust size distribution and hence MEE may change. In this study we have also assumed that dust MEE does not change during the course of trans-Atlantic transport. Some observations have shown that dust MEE increases by about 15% from the African coast to the Caribbean (Chen et al., 2011; Maring et al., 2003), although more measurements are needed to further assess the evolution of dust properties during the long-range transport (Formenti et al., 2011; Mahowald et al., 2014). Here we assume that the assumption of constant dust size distribution during the trans-Atlantic transport would cause an uncertainty of $\pm 15\%$ in the dust mass flux.

By cumulating the individual known uncertainties discussed above, we estimate that the overall known uncertainty in the estimated dust mass flux is $\pm(45\text{--}70)\%$ (see Table 7), with the lower uncertainty near the African coast and higher uncertainty in the Caribbean Sea. We note that additional uncertainty may arise from the missing below-cloud aerosols in the CALIOP measurements, the use of nighttime data only, and CALIOP limited spatial sampling. However, such uncertainty cannot be robustly assessed because of lack of observations and inconsistent data quality of CALIOP daytime and nighttime measurements.

Table 7

Summary of major sources of uncertainty in the estimated dust mass flux. *f* represents uncertainty factor, with a value of 1 indicating zero uncertainty. The overall uncertainty factor is calculated as a product of individual *f* values.

Uncertainty source	Estimated relative uncertainty	Notes
CALIP AOD	−30% (biased low) (<i>f</i> = 0.70)	Schuster et al. (2012), Omar et al. (2013), Liu et al. (2014)
CALIP vertical profile shape	±10% (<i>f</i> = 1.10)	Winker et al. (2009), Yu et al. (2010)
CALIP dust and non-dust separation	±(15–34)% (<i>f</i> = 1.15–1.34)	Estimated according to the LDF and UDF scenarios (Table 2); lower uncertainty near the source and higher uncertainty far away from the source (in Caribbean)
Dust MEE	+30% (biased high) (<i>f</i> = 1.30)	Chen et al. (2011), Ansmann et al. (2012)
Unchanged dust size distribution	±15% (<i>f</i> = 1.15)	Maring et al. (2003), Chen et al. (2011)
Missing of below-cloud aerosols	Unknown	No observations are available to assess, as discussed in Section 4.1.
Use of nighttime data only	Unknown	CALIP nighttime data are more accurate than daytime data. Because of their different data qualities, it is impossible to associate any examined day-night difference (Section 4.2) with physical processes.
Overall <i>known</i> uncertainty	±(45–70)% (<i>f</i> = 1.45–1.70)	By cumulating all known uncertainties listed above

5. Conclusions

Quantifying the transport of dust from source to remote regions is essential to understanding a variety of far-reaching impacts of dust on human and ecosystem health, the terrestrial and oceanic biogeochemical cycles, and weather and climate. This task can only be accomplished with satellite measurements that provide routine sampling of aerosols in the troposphere and stratosphere over a hemispheric or global scale. In this study we have taken advantage of the 7-year (2007–2013) record of CALIPSO lidar observations of the three-dimensional distribution of aerosols in both clear and cloudy conditions to address several assumptions associated with the previous MODIS-based estimate (Kaufman et al., 2005). We have provided an independent, multi-year estimate of trans-Atlantic dust transport in the zonal direction based on the CALIP observations. Specifically, CALIP observations of aerosol extinction were partitioned into dust and non-dust aerosols based on observed depolarization ratios with a priori knowledge of characteristic depolarization ratios for dust and non-dust aerosols. For the first time both cloud-free and above-cloud aerosol profiles have been used to estimate the vertically resolved dust mass flux in all sky conditions.

We estimated that on the basis of the 7-year average and an integration over the 10°S–30°N latitudinal strip, 182 Tg a^{−1} dust is transported to 15°W near the coast of North Africa, of which 132 Tg a^{−1} and 43 Tg a^{−1} reaches 35°W and 75°W, respectively. These fluxes represent the best estimate of dust mass fluxes by averaging results from the upper-bound dust fraction (UDF) and lower-bound dust fraction (LDF) scenarios. The estimated dust mass fluxes have an overall known uncertainty of ±(45–70)%, resulting from uncertainties/biases associated with CALIP AOD and vertical profile, the dust and non-dust separation schemes, and dust mass extinction efficiency assumptions. Because of the lack of reliable observations, uncertainties associated with the diurnal variation of dust, the missing below-cloud dust, and CALIP limited spatial sampling cannot be quantified.

The MODIS-based dust flux estimates (Kaufman et al., 2005) integrated over the 10°S–30°N generally agree well with the CALIP-based estimates. At 35°W, the MODIS-based estimate of 126 Tg a^{−1} is close to the best estimate of 132 Tg a^{−1} from CALIP observations. At the cross section of 15°W and 75°W, the MODIS-estimated dust flux of 233 and 58 Tg a^{−1} respectively agrees well with the CALIP upper-bound estimate. On the other hand, larger differences are observed in the meridional distribution of dust zonal flux between CALIP and MODIS. For example, at the 15°W cross section the MODIS flux in 10°–20°N is more than a factor of 3 larger than that in 0°–10°N. However, such meridional difference is only 30–50% for the CALIP flux.

The trans-Atlantic dust transport shows significant seasonal variations. The dust mass flux is the highest in summer and the lowest in

fall. There is seasonal shift in meridional distribution of dust transport, which is largely controlled by the advance and retreat of the ITCZ. In winter and spring, dust transport shifts southward to 0°–10°N and affects South America significantly. In summer, the dust transport occurs predominantly at 10°–20°N and affects the Caribbean Sea substantially. CALIP's unique observations of dust vertical profiles reveal that the relative contributions of dust mass flux from different seasons change with altitude. At 15°W and 35°W, the annual dust mass flux is dominated by contributions from DJF and MAM at altitudes lower than 2–3 km, but in JJA the dust transport occurs at higher altitudes. Dust mass flux occurs above 4 km only in JJA. At 75°W, the dust mass flux is consistently higher in JJA than other seasons at all altitudes.

The dust mass flux also shows large interannual variations, with the year-to-year variation up to 86% in the period of 2007–2013. We showed that the interannual variations are associated with large-scale circulations as represented by the NAO index and Sahel Precipitation Index (SPI). In the winter season, the dust mass flux is positively correlated with the winter NAO index, with a correlation coefficient *R* of 0.80, 0.83, and 0.70 at 15°W, 35°W, and 75°W, respectively. The annual dust mass fluxes at all the three longitudinal cross-sections are highly anti-correlated with prior-year SPI with respective *R*² of 0.86, 0.59, and 0.82, suggesting that the prior-year SPI may be a good indicator for the trans-Atlantic dust transport.

CALIP's unique capability of profiling above-cloud aerosols (ACA) allows us for the first time to examine potential bias associated with the use of only clear-sky aerosol (CSA) measurements in calculating the dust mass flux. We found that the use of CSA observation only would introduce an overestimate of about 20% in the Northern Hemisphere winter and spring at the 35°W and 75°W cross sections, based on the 7-year average. In one particular year, the overestimate was as high as 42%. On the other hand, the corresponding difference at 15°W is relatively small (generally within 10%). However, these assessments are limited by CALIP's inability to detect aerosols below low-level clouds and the use of CALIP ACA fraction at nighttime. Future analysis with ground-based lidars for quantifying the below-cloud aerosol and full characterization of diurnal variations of the ACA fraction could provide deeper insight.

Acknowledgments

The work was supported by the NASA CALIPSO/CloudSat project (NNX14AB21G) managed by Dr. David Considine and the Science of Terra and Aqua project (NNX11AH66G) managed by Dr. Richard Eckman. The CALIPSO data were obtained from the NASA Langley Research Center Atmospheric Sciences Data Center (https://eosweb.larc.nasa.gov/project/calipso/calipso_table). We thank Pls of AERONET Cape Verde and La Parguera sites for collecting the data (<http://>

aeronnet/cgi-bin/webtool_opera_v2_new) that are used in this study. The authors gratefully acknowledge the NOAA Air Resources Laboratory (ARL) for the provision of the HYSPLIT transport and dispersion model and READY website (<http://www.ready.noaa.gov>) used in this publication.

References

- Adams, A.M., Prospero, J.M., & Zhang, C. (2012). CALIPSO-derived three-dimensional structure of aerosol over the Atlantic basin and adjacent continents. *Journal of Climate*, 25, 6862–6879.
- Ansmann, A., Seifert, P., Tesche, M., & Wandinger, U. (2012). Profiling of fine and coarse particle mass: Case studies of Saharan dust and Eyjafjallajökull/Grimsvotn volcanic plumes. *Atmospheric Chemistry and Physics*, 12, 9399–9415.
- Ben-Ami, Y., Koren, I., & Altaratz, O. (2009). Patterns of North African dust transport over the Atlantic: Winter vs. summer, based on CALIPSO first year data. *Atmospheric Chemistry and Physics*, 9, 7867–7875. <http://dx.doi.org/10.5194/acp-9-7867-2009>.
- Ben-Ami, Y., Koren, I., Altaratz, O., & Lehahn, Y. (2012). Discernable rhythm in the spatial/temporal distributions of transatlantic dust. *Atmospheric Chemistry and Physics*, 12, 2253–2262.
- Ben-Ami, Y., Koren, I., Rudich, Y., Artaxo, P., Martin, S.T., & Andreae, M.O. (2010). Transport of North African dust from the Bodele depression to the Amazon Basin: A case study. *Atmospheric Chemistry and Physics*, 10, 7533–7544. <http://dx.doi.org/10.5194/acp-10-7533-2010>.
- Bristow, C. S., Hudson-Edwards, K. A., & Chappell, A. (2010). Fertilizing the Amazon and equatorial Atlantic with West African dust. *Geophysical Research Letters*, 37, L14807. <http://dx.doi.org/10.1029/2010GL043486>.
- Burton, S.P., Ferrare, R.A., Hostetler, C.A., Hair, J.W., Rogers, R.R., Obland, M.D., et al. (2012). Aerosol classification using airborne High Spectral Resolution Lidar measurements – Methodology and examples. *Atmospheric Measurement Techniques*, 5, 73–98.
- Chen, G., Ziemba, L.D., Chu, D.A., Thornhill, K.L., Schuster, G.L., Winstead, E.L., et al. (2011). Observations of Saharan dust microphysical and optical properties from the Eastern Atlantic during NAMMA airborne field campaign. *Atmospheric Chemistry and Physics*, 11, 723–740.
- Cheng, Y.-S., Yeh, H.-C., & Allen, M.D. (1988). Dynamic shape factor of a plate-like particle. *Aerosol Science and Technology*, 8, 109–123.
- Chiappello, I., & Moulin, C. (2002). TOMS and Meteosat satellite records of the variability of Saharan dust transport over the Atlantic during the last two decades (1979–1997). *Geophysical Research Letters*, 29, 1176. <http://dx.doi.org/10.1029/2001GL013767>.
- Chiappello, I., Moulin, C., & Prospero, J.M. (2005). Understanding the long-term variability of African dust transport across the Atlantic as recorded in both Barbados surface concentrations and large-scale Total Ozone Mapping Spectrometer (TOMS) optical thickness. *Journal of Geophysical Research*, 110, D18S10. <http://dx.doi.org/10.1029/2004JD005132>.
- Chiappello, I., et al. (1997). Origins of African dust transported over the northeastern tropical Atlantic. *Journal of Geophysical Research*, 102, 13,701–13,709. <http://dx.doi.org/10.1029/97JD00259>.
- Chin, M., Diehl, T., Tan, Q., Prospero, J.M., Kahn, R.A., Remer, L.A., et al. (2014). Multi-decadal aerosol variations from 1980 to 2009: A perspective from observations and a global model. *Atmospheric Chemistry and Physics*, 14, 1657–3690.
- Doherty, O.M., Riemer, N., & Hameed, S. (2012). Control of Saharan mineral dust transport to Barbados in winter by the Intertropical Convergence Zone over West Africa. *Journal of Geophysical Research*, 117, D19117. <http://dx.doi.org/10.1029/2012JD017767>.
- Draxler, R.R., & Rolph, G.D. (2014). HYSPLIT (HYbrid Single-Particle Lagrangian Integrated Trajectory) Model access via NOAA ARL READY Website (<http://www.arl.noaa.gov/HYSPLIT.php>). College Park, MD: NOAA Air Resources Laboratory.
- Dunion, J., & Velden, C. (2004). The impact of the Saharan air layer on Atlantic tropical cyclone activity. *Bulletin of the American Meteorological Society*, 85, 353–356. <http://dx.doi.org/10.1175/BAMS-85-3-353>.
- Esselborn, M., Wirth, M., Fix, A., Weinzier, B., Rasp, K., Tesche, M., et al. (2009). Spatial distribution and optical properties of Saharan dust observed by airborne high spectral resolution lidar during SAMUM 2006. *Tellus*, 61B, 131–143.
- Evan, A. T., Vimont, D. J., Heidinger, A. K., Kossin, J. P., & Bennartz, R. (2009). The role of aerosols in the evolution of tropical North Atlantic Ocean temperature anomalies. *Science*, 324, 778–781. <http://dx.doi.org/10.1126/science.1167404>.
- Fiebig, M., Petzold, A., Wandinger, U., Wendisch, M., Kiemle, C., Stifter, A., et al. (2002). Optical closure for an aerosol column: Method, accuracy, and inferable properties applied to a biomass-burning aerosol and its radiative forcing. *Journal of Geophysical Research*, 107, 810. <http://dx.doi.org/10.1029/2000JD000192>.
- Formenti, P., Schutz, L., Balkanski, Y., Desbois, K., Ebert, M., Kandler, K., et al. (2011). Recent progress in understanding physical and chemical properties of African and Asian mineral dust. *Atmospheric Chemistry and Physics*, 11, 8231–8256.
- Freudenthaler, V., Esselborn, M., Wiegner, M., Heese, B., Tesche, M., Ansmann, A., et al. (2009). Depolarization-ratio profiling at several wavelengths in pure Saharan dust during SAMUM 2006. *Tellus*, 61B, 165–179.
- Generoso, S., Bey, I., Labonne, M., & Bréon, F.-M. (2008). Aerosol vertical distribution in dust outflow over the Atlantic: Comparisons between GEOS-Chem and Cloud-Aerosol Lidar and Infrared Pathfinder Satellite Observation (CALIPSO). *Journal of Geophysical Research*, 113, D24209. <http://dx.doi.org/10.1029/2008JD010154>.
- Ginoux, P., Prospero, J.M., Torres, O., & Chin, M. (2004). Long-term simulation of global dust distribution with the GOCART model: Correlation with North Atlantic oscillation. *Environmental Modelling & Software*, 19, 113–128.
- Griffin, D.W. (2007). Atmospheric movement of microorganisms in clouds of desert dust and implications for human health. *Clinical Microbiology*, 20, 459–477.
- Guo, Y., Tian, B., Kahn, R.A., Kalashnikova, O., Wong, S., & Waliser, D.E. (2013). Tropical Atlantic dust and smoke aerosol variations related to the Madden-Julian Oscillation in MODIS and MISR observations. *Journal of Geophysical Research – Atmospheres*, 118, 4947–4963. <http://dx.doi.org/10.1002/jgrd.50409>.
- Hayasaka, T., Satake, S., Shimizu, A., Sugimoto, N., Matsui, I., Aoki, K., et al. (2007). Vertical distribution and optical properties of aerosols observed over Japan during the Atmospheric Brown Clouds – East Asia Regional Experiment 2005. *Journal of Geophysical Research*, 112, D22S35. <http://dx.doi.org/10.1029/2006JD008086>.
- Haywood, J., Francis, P., Osborne, S., Glew, M., Loeb, N., Highwood, E., et al. (2003). Radiative properties and direct radiative effect of Saharan dust measured by the C-130 aircraft during SHADE: 1. Solar spectrum. *Journal of Geophysical Research*, 108, 8577. <http://dx.doi.org/10.1029/2002JD002687>.
- Hess, M., Koepke, P., & Schult, I. (1998). Optical properties of aerosols and clouds: The software package OPAC. *Bulletin of the American Meteorological Society*, 79, 831–844.
- Hu, Y. (2007). Depolarization ratio-effective lidar ratio relation: Theoretical basis for space lidar cloud phase discrimination. *Geophysical Research Letters*, 34, L11812. <http://dx.doi.org/10.1029/2007GL029584>.
- Huang, J., Zhang, C., & Prospero, J.M. (2010). African dust outbreaks: A satellite perspective of temporal and spatial variability over the tropical Atlantic Ocean. *Journal of Geophysical Research*, 115, D05202. <http://dx.doi.org/10.1029/2009JD012516>.
- Huneen, N., Schulz, M., Balkanski, Y., Griesfeller, J., Prospero, J., Kinne, S., et al. (2011). Global dust model intercomparison in AeroCom phase I. *Atmospheric Chemistry and Physics*, 11, 7781–7816.
- Hurrell, J.W. (1995). Decadal trend in the North Atlantic Oscillation: Regional temperatures and precipitations. *Science*, 269, 676–679.
- Janowiak, J.E. (1988). An investigation of interannual rainfall variability in Africa. *Journal of Climate*, 1, 240–255.
- Jickells, T.D., An, Z.S., Andersen, K.K., Baker, A.R., Bergametti, G., Brooks, N., et al. (2005). Global iron connections between desert dust, ocean biogeochemistry, and climate. *Science*, 308, 67–71. <http://dx.doi.org/10.1126/science.1105959>.
- Kalashnikova, O.V., & Kahn, R. (2008). Mineral dust plume evolution over the Atlantic from combined MISR/MODIS aerosol retrievals. *Journal of Geophysical Research*, 113, D24204. <http://dx.doi.org/10.1029/2008JD010083>.
- Kalu, A.E. (1979). The African dust plume: Its characteristics and propagation across West Africa in winter. *Scope*, 14, 95–118.
- Kaufman, Y.J., Koren, I., Remer, L.A., Tanré, D., Ginoux, P., & Fan, S. (2005). Dust transport and deposition observed from the Terra-Moderate Resolution Imaging Spectroradiometer (MODIS) spacecraft over the Atlantic Ocean. *Journal of Geophysical Research*, 110, D10S12. <http://dx.doi.org/10.1029/2003JD004436>.
- Kim, D., Chin, M., Yu, H., Diehl, T., Tan, Q., Kahn, R.A., et al. (2014). Sources, sinks, and transatlantic transport of North African dust aerosol: A multi-model analysis and comparison with remote-sensing data. *Journal of Geophysical Research – Atmospheres*, 119, 6259–6277. <http://dx.doi.org/10.1002/2013JD021099>.
- Koren, I., Kaufman, Y.J., Washington, R., Todd, M.C., Rudich, Y., Martins, J.V., et al. (2006). The Bodele depression: A single spot in the Sahara that provides most of the mineral dust to the Amazon forest. *Environmental Research Letters*, 1(1), 014005. <http://dx.doi.org/10.1088/1748-9326/1/1/014005>.
- Liu, Z., Omar, A., Vaughan, M., Hair, J., Kittaka, C., Hu, Y., et al. (2008). CALIPSO lidar observations of the optical properties of Saharan dust: A case study of long-range transport. *Journal of Geophysical Research*, 113, D07207. <http://dx.doi.org/10.1029/2007JD008878>.
- Liu, Z., Winker, D., Omar, A., Vaughan, M., Kar, J., Treppe, C., et al. (2014). Evaluation of CALIOP 532 nm AOD over opaque water clouds. *Atmospheric Chemistry and Physics Discussions*, 14, 23583–23637.
- Mahowald, N., Albani, S., Kok, J.F., Engelstaedter, S., Scanza, R., Ward, D.S., et al. (2014). The size distribution of desert dust aerosols and its impact on the Earth system. *Aeolian Research*, 15, 53–71. <http://dx.doi.org/10.1016/j.aeolia.2013.09.002>.
- Mahowald, N., Jickells, T.D., Baker, A.R., Artaxo, P., Benitez-Nelson, C.R., Bergametti, G., et al. (2008). The global distribution of atmospheric phosphorus deposition and anthropogenic impacts. *Global Biogeochemical Cycles*, 22, GB4026. <http://dx.doi.org/10.1029/2008GB003240>.
- Maring, H., Savoie, D.L., Izaguirre, M.A., Custals, L., & Reid, J.S. (2003). Mineral dust aerosol size distribution change during atmospheric transport. *Journal of Geophysical Research*, 108(D19), 8592. <http://dx.doi.org/10.1029/2002JD002536>.
- Moulin, C., Lambert, C.E., Dulac, F., & Dayan, U. (1997). Control of atmospheric export of dust from North Africa by the North Atlantic Oscillation. *Nature*, 387, 691–694.
- Omar, A., Liu, Z., Vaughan, M., Thornhill, K., Kittaka, C., Ismail, S., et al. (2010). Extinction-to-backscatter ratios of Saharan dust layers derived from in situ measurements and CALIPSO overflights during NAMMA. *Journal of Geophysical Research*, 115, D24217. <http://dx.doi.org/10.1029/2010JD014223>.
- Omar, A.H., Winker, D.M., Tackett, J.L., Giles, D.M., Kar, J., Liu, Z., et al. (2013). CALIOP and AERONET aerosol optical depth comparisons: One size fits none. *Journal of Geophysical Research – Atmospheres*, 118, 4748–4766. <http://dx.doi.org/10.1002/jgrd.50330>.
- Omar, A.H., Winker, D.M., Vaughan, M.A., Hu, Y., Treppe, C.R., Ferrare, R.A., et al. (2009). The CALIPSO automated aerosol classification and lidar ratio selection algorithm. *Journal of Atmospheric and Oceanic Technology*, 26, 1994–2014. <http://dx.doi.org/10.1175/2009JTECHA1231.1>.
- Peyridieu, S., Chedin, A., Tanre, D., Capelle, V., Pierangelo, C., Lamquin, N., et al. (2010). Saharan dust infrared optical depth and altitude retrieved from AIRS: A focus over North Atlantic – comparisons to MODIS and CALIPSO. *Atmospheric Chemistry and Physics*, 10, 1953–1967.
- Prospero, J.M. (1999). Long-term measurements of the transport of African mineral dust to the southeastern United States: Implications for regional air quality. *Journal of Geophysical Research*, 104, 15,917–15,927. <http://dx.doi.org/10.1029/1999JD900072>.

- Prospero, J.M., Barrett, K., Church, T., Dentener, F., Duce, R.A., Galloway, J.N., et al. (1996). Atmospheric deposition of nutrients to the North Atlantic Basin. *Biogeochemistry*, 35, 27–73. <http://dx.doi.org/10.1007/BF02179824>.
- Prospero, J.M., Blades, E., Mathison, G., & Naidu, R. (2005). Interhemispheric transport of viable fungi and bacteria from Africa to the Caribbean with soil dust. *Aerobiologia*, 21, 1–19. <http://dx.doi.org/10.1007/s10453-004-5872-7>.
- Prospero, J.M., Collard, F.-X., Molinié, J., & Jeannot, A. (2014). Characterizing the annual cycle of African dust transport to the Caribbean Basin and South America and its impact on the environment and air quality. *Global Biogeochemical Cycles*, 29, 757–773. <http://dx.doi.org/10.1002/2013GB004802>.
- Prospero, J.M., & Lamb, P.J. (2003). African droughts and dust transport to the Caribbean: Climate change implications. *Science*, 302, 1024–1027.
- Prospero, J.M., Landing, W.M., & Schulz, M. (2010). African dust deposition to Florida: Temporal and spatial variability and comparisons to models. *Journal of Geophysical Research*, 115, D13304. <http://dx.doi.org/10.1029/2009JD012773>.
- Reid, E.A., Reid, J.S., Meier, M.M., Dunlap, M.R., Cliff, S.S., Broumas, A., et al. (2003). Characterization of African dust transported to Puerto Rico by individual particle and size segregated bulk analysis. *Journal of Geophysical Research*, 108, 8591. <http://dx.doi.org/10.1029/2002JD002935>.
- Ridley, D.A., Heald, C.L., & Ford, B. (2012). North African dust export and deposition: A satellite and model perspective. *Journal of Geophysical Research*, 117, D02202. <http://dx.doi.org/10.1029/2011JD016794>.
- Riemer, N., Doherty, O.M., & Hameed, S. (2006). On the variability of African dust transport across the Atlantic. *Geophysical Research Letters*, 33, L13814. <http://dx.doi.org/10.1029/2006GL026163>.
- Rienecker, M., Suarez, M.J., Gelaro, R., Todling, R., Bacmeister, J., Liu, E., et al. (2011). MERRA: NASA's modern-era retrospective analysis for research and applications. *Journal of Climate*, 24, 3624–3648.
- Rudich, Y., Kaufman, Y.J., Dayan, U., Yu, H., & Kleidman, R.G. (2008). Estimation of transboundary transport of pollution aerosols by remote sensing in the eastern Mediterranean. *Journal of Geophysical Research*, 113, D14S13. <http://dx.doi.org/10.1029/2007JD009601>.
- Sakai, T., Nagai, T., Zaizen, Y., & Mano, Y. (2010). Backscattering linear depolarization ratio measurements of mineral, sea-salt, and ammonium sulfate particles simulated in a laboratory chamber. *Applied Optics*, 49, 4441–4449.
- Schepanski, K., Tegen, I., & Macke, A. (2009). Saharan dust transport and deposition towards the tropical northern Atlantic. *Atmospheric Chemistry and Physics*, 9, 1173–1189. <http://dx.doi.org/10.5194/acp-9-1173-2009>.
- Schuster, G.L., Vaughan, M., MacDonnell, D., SU, W., Winker, D., Dubovik, O., et al. (2012). Comparison of CALIPSO aerosol optical depth retrievals to AERONET measurements, and a climatology of lidar ratio of dust. *Atmospheric Chemistry and Physics*, 12, 7431–7452.
- Shao, Y., Wyrwoll, K.-H., Chappell, A., Huang, J., Lin, Z., McTainsh, G.H., et al. (2011). Dust cycle: An emerging core theme in Earth system science. *Aeolian Research*, 2, 181–204.
- Smirnov, A., Holben, B.N., Eck, T.F., Slutsker, I., Chatenet, B., & Pinker, R.T. (2002). Diurnal variability of aerosol optical depth observed at AERONET (Aerosol Robotic Network) sites. *Geophysical Research Letters*, 29, 2115. <http://dx.doi.org/10.1029/2002GL016305>.
- Su, L., & Toon, O.B. (2011). Saharan and Asian dust: Similarities and differences determined by CALIPSO, AERONET, and a coupled climate-aerosol microphysical model. *Atmospheric Chemistry and Physics*, 11, 3263–3280. <http://dx.doi.org/10.5194/acp-11-3263-2011>.
- Swap, R., Garstang, M., Greco, S., Talbot, R., & Källberg, P. (1992). Saharan dust in the Amazon Basin. *Tellus Series B*, 44, 133–149. <http://dx.doi.org/10.1034/j.1600-0889.1992.t01-1-00005.x>.
- Swap, R., Ulanski, S., Cobbett, M., & Garstang, M. (1996). Temporal and spatial characteristics of Saharan dust outbreaks. *Journal of Geophysical Research*, 101(D2), 4205–4220.
- Wilcox, E.M., Lau, K.-M., & Kim, K.-M. (2010). A northward shift of the North Atlantic Ocean Intertropical Convergence Zone in response to summertime Saharan dust outbreaks. *Geophysical Research Letters*, 37, L04804. <http://dx.doi.org/10.1029/2009GL041774>.
- Winker, D.M., Tackett, J.L., Getzewich, B.J., Liu, Z., Vaughan, M.A., & Rogers, R.R. (2013). The global 3-D distribution of tropospheric aerosols as characterized by CALIOP. *Atmospheric Chemistry and Physics*, 13, 3345–3361. <http://dx.doi.org/10.5194/acp-13-3345-2013>.
- Winker, D., Vaughan, M.A., Omar, A., Hu, Y.X., Powell, K.A., Liu, Z.Y., et al. (2009). Overview of the CALIPSO mission and CALIOP data processing algorithms. *Journal of Atmospheric and Oceanic Technology*, 26(11), 2310–2323.
- Yang, W., Marshak, A., Kostinski, A.B., & Várnai, T. (2013). Shape-induced gravitational sorting of Saharan dust during transatlantic voyage: Evidence from CALIOP lidar depolarization measurements. *Geophysical Research Letters*, 40, 3281–3286. <http://dx.doi.org/10.1002/grl.50603>.
- Yu, H., Chin, M., Remer, L.A., Kleidman, R.G., Bellouin, N., Bian, H., et al. (2009). Variability of marine aerosol fine-mode fraction and estimates of anthropogenic aerosol component over cloud-free oceans from the Moderate Resolution Imaging Spectroradiometer (MODIS). *Journal of Geophysical Research*, 114, D10206. <http://dx.doi.org/10.1029/2008JD010648>.
- Yu, H., Chin, M., Winker, D.M., Omar, A.H., Liu, Z., Kittaka, C., et al. (2010). Global view of aerosol vertical distributions from CALIPSO lidar measurements and GOCART simulations: Regional and seasonal variations. *Journal of Geophysical Research*, 115, D00H30. <http://dx.doi.org/10.1029/2009JD013364>.
- Yu, H., Remer, L.A., Chin, M., Bian, H., Kleidman, R.G., & Diehl, T. (2008). A satellite-based assessment of transpacific transport of pollution aerosol. *Journal of Geophysical Research*, 113, D14S12. <http://dx.doi.org/10.1029/2007JD009349>.
- Yu, H., Remer, L.A., Chin, M., Bian, H., Tan, Q., Yuan, T., et al. (2012). Aerosols from overseas rival domestic emissions over North America. *Science*, 337, 566–569. <http://dx.doi.org/10.1126/science.1217576>.
- Yu, H., Remer, L.A., Kahn, R.A., Chin, M., & Zhang, Y. (2013). Satellite perspective of aerosol intercontinental transport: From qualitative tracking to quantitative characterization. *Atmospheric Research*, 124, 73–100. <http://dx.doi.org/10.1016/j.atmosres.2012.12.013>.
- Yu, H., & Zhang, Z. (2013). New directions: Emerging satellite observations of above-cloud aerosols and direct radiative forcing. *Atmospheric Environment*, 72, 36–40. <http://dx.doi.org/10.1016/j.atmosenv.2013.02.17>.
- Yu, H., Zhang, Y., Chin, M., Liu, Z., Omar, A., Remer, L.A., et al. (2012). An integrated analysis of aerosol above clouds from A-Train multi-sensor measurements. *Remote Sensing of Environment*, 121, 125–131.
- Zhang, Y., Yu, H., Eck, T.F., Smirnov, A., Chin, M., Remer, L.A., et al. (2012). Aerosol daytime variations over North and South America derived from multiyear AERONET measurements. *Journal of Geophysical Research*, 117, D05211. <http://dx.doi.org/10.1029/2011JD017242>.